Surveying the Giant H II Regions of the Milky Way with SOFIA. IV. Sgr D, W42, and a Reassessment of the Giant H II Region Census

James M. De Buizer[ID], Wanggi Lim[ID], Nicole Karnath[ID], James T. Radomski[ID], and Lars Bonne[ID]
SOFIA-USRA, NASA Ames Research Center, MS 232-12, Moffett Field, CA 94035, USA; jdebuizer@sofia.usra.edu

Abstract

This is the fourth paper exploring the infrared properties of giant H II regions with the FORCAST instrument on the Stratospheric Observatory For Infrared Astronomy (SOFIA). Our survey utilizes the census of 56 Milky Way giant H II regions identified by Conti & Crowther, and in this paper we present the 20 and 37 μm imaging data we obtained from SOFIA for sources Sgr D and W42. Based upon the SOFIA data and other multiwavelength data, we derive and discuss the detailed physical properties of the individual compact sources and subregions as well as the large-scale properties of Sgr D and W42. However, improved measurements have revealed much closer distances to both regions than previously believed, and consequently, both sources are not powerful enough to be considered giant H II regions any longer. Motivated by this, we revisit the census of giant H II regions, performing a search of the last two decades of literature to update each source with the most recent and/or most accurate distance measurements. Based on these new distance estimates, we determine that 14 sources in total (25%) are at sufficiently reliable and closer distances that they are not powerful enough to be considered giant H II regions. We briefly discuss the observational and physical characteristics specific to Sgr D and W42 and show that they have properties distinct from the giant H II regions previously studied as a part of this survey.

Unified Astronomy Thesaurus concepts: H II regions (694); Infrared sources (793); Star forming regions (1565); Young star clusters (1833)

1. Introduction

This is the fourth paper in a series of studies of the properties of Milky Way giant H II (GH II) regions, which represent the largest and most powerful star-forming areas of the Galaxy. Regions such as these dominate the emission of most galaxies, and therefore GH II regions are laboratories for understanding large-scale star formation within galaxies in general (Shields 1990). As their moniker implies, the large clusters of high-mass stars and protostars within GH II regions provide a tremendous supply of ionizing (i.e., Lyman continuum) photons that create vast, bright, and optically thin centimeter radio continuum regions. For example, M17 has a radio continuum diameter of over 10 pc and contains ∼100 O and B-type stars (Hoffmeister et al. 2008).

Because these regions are so bright in the mid-infrared, the highest spatial resolution images from space missions like the Spitzer Space Telescope and the Wide-field Infrared Survey Explorer (WISE) are saturated over most of their emitting areas at wavelengths ⩾15 μm. While some sources and subregions within some GH II regions have been imaged at (sub-)arcsecond resolution via ground-based mid-infrared facilities (e.g., Smith et al. 2000; Kassis et al. 2002; Barbosa et al. 2016), there are technical limitations (like small fields of view) that make it impractical to make the large maps required to fully cover the entire mid-infrared-emitting area of these GH II regions, many of which are more than 4′ in diameter. To date, the most complete maps in the mid-infrared are from the Midcourse Space Experiment (MSX), which have a spatial resolution of only ∼18″ at 22 μm. Our survey source list comes from the census of Conti & Crowther (2004), who identified 56 GH II regions in our Galaxy based on their 6 cm radio and mid-infrared (via MSX data) fluxes. Though this census contains the brightest star-forming regions in the Galaxy, it is not considered a complete survey of the entire population of radio GH II regions. Nevertheless, the ultimate goal of our project is to compile a 20 and 37 μm imaging survey of as many GH II regions within the Milky Way as we can with the Stratospheric Observatory For Infrared Astronomy (SOFIA) and its mid-infrared instrument FORCAST, creating complete and unsaturated maps of these regions with the best resolution ever achieved at our longest wavelength (i.e., ∼3″ at 37 μm). From our infrared observations we will gain a better understanding of their physical properties individually and as a population.

In this paper we will, in part, concentrate on the SOFIA data we have obtained for sources Sgr D and W42. Though these sources are from the GH II region census from Conti & Crowther (2004), more recent and/or more accurate measurements of the distances to both of these sources have shown that both are much closer to the Sun than previously believed. GH II regions possess a Lyman continuum photon rate, N_{LyC}, of greater than 10^{50} photons s^{-1} (Mezger 1970; Conti & Crowther 2004), and the derivation of this value is dependent upon source distance. We will show in this paper that recalculating N_{LyC} using the new, closer distances for both Sgr D and W42 indicate that neither qualifies as a GH II region under the above criterion.

As these regions are not GH II regions, we will not go into the same depth of analyses as we have for our previous papers in this survey. However, since we have obtained SOFIA data on both of these regions, we were motivated to see what could be learned by comparing and contrasting their properties to those of the most luminous GH II regions we have previously studied. Therefore, the first goal of this paper is to derive the

physical properties for the individual sources and subregions that make up both Sgr D and W42, and to quantify the nature of these regions as a whole.

However, given the importance of distance on the classification of our source list as bona fide GH II regions, and given the almost two decades that have past since that census was published, we were compelled to perform a literature search for the remaining Conti & Crowther (2004) sources to compile the latest distance estimates for each source and recalculate their Lyman continuum photon rates to see which sources still qualify as GH II regions. The distances to most of these sources had previously only been determined through kinematic methods, which are notoriously unreliable. Being sites for the formation of some of the most massive stars in the Galaxy means that GH II regions often contain massive young stellar objects (MYSOs) displaying maser activity, and this has led to a host of studies in the past decade that utilize the masers to obtain accurate trigonometric parallax measurements to such regions. Other methods, such as spectrophotometry as well as stellar parallax measurements from the Global Astrometric Interferometer for Astrophysics mission (GAIA), have also been utilized to obtain more accurate distance measurements to these regions in the almost two decades since Conti & Crowther (2004). Therefore, the second goal of this paper is to create an updated census of GH II regions to serve as the source list for our survey moving forward.

This paper is organized in the following manner. In Section 2, we will discuss the SOFIA observations and data reduction and analyses for both Sgr D and W42, including the creation and modeling of the infrared spectral energy distributions (SEDs) for sources within each region. We will provide more background on both regions as we compare our new data to previous observations and briefly discuss the nature of each region and discuss individual sources and subregions in-depth in Sections 3 (Sgr D) and 4 (W42). In Section 5 we discuss in detail the reassessment of the Conti & Crowther (2004) census, including discussions of the methods used to determine distances to the entire list of GH II regions, explanation of the calculation of Lyman continuum photon rate, and discussion of details related to the final list of updated GH II regions. In Section 6, we examine the nature of rejected GH II region sources Sgr D and W42 and investigate the their physical properties (beyond just the Lyman continuum photon rate) and how they compare to the sources we have previously studied with SOFIA that are bona fide GH II regions. We summarize our results in Section 7.

2. Observations, Data Reduction, and Analyses

The SOFIA data for these sources were obtained in the same manner as for those in our previous three papers, and we direct the reader to the discussion of those details in Paper I (i.e., Lim & De Buizer 2019). We will highlight below some of observation and reduction details specific to the Sgr D and W42 observations.

The data for Sgr D were obtained during SOFIA's Cycle 3 using the FORCAST instrument (Herter et al. 2013) on the night of 2015 June 24 (Flight 221). FORCAST is a dual-array mid-infrared camera capable of taking simultaneous images at two wavelengths. The short wavelength camera (SWC) is a 256×256 pixel Si:As array optimized for 5–$25\,\mu$m observations; the long wavelength camera (LWC) is a 256×256 pixel Si:Sb array optimized for 25–$40\,\mu$m observations. After correction for focal plane distortion, FORCAST effectively samples at $0\rlap{.}''768$ pixel^{-1}, which yields a $3\rlap{.}'4 \times 3\rlap{.}'2$ instantaneous field of view. Observations of Sgr D were obtained using the $20\,\mu$m ($\lambda_{\rm eff} = 19.7\,\mu$m; $\Delta\lambda = 5.5\,\mu$m) and $37\,\mu$m ($\lambda_{\rm eff} = 37.1\,\mu$m; $\Delta\lambda = 3.3\,\mu$m) filters simultaneously using an internal dichroic. Data were obtained at aircraft altitude of 36,000 feet by employing the standard chop-nod observing technique used in the thermal infrared, with $3'$ chop and nod throws and an on-source integration time of about $450\,$s in both filters.

For W42, data were obtained during SOFIA's Cycle 2 on the night of 2014 June 4 (Flight 176). A different filter was used in the short wavelength camera of FORCAST for these earlier observations of our project, namely, the $25\,\mu$m ($\lambda_{\rm eff} = 25.3\,\mu$m; $\Delta\lambda = 1.9\,\mu$m) filter. However, the dichroic mode was still employed so that these observations were taken simultaneously with the same $37\,\mu$m filter as was used for the Sgr D observations. Data were obtained at aircraft altitude of 43,000 feet with $5'$ chop and nod throws. Unlike Sgr D, the mid-infrared-emitting region of W42 is larger ($\sim 4\rlap{.}'5 \times 4\rlap{.}'5$) than the FORCAST field of view, and thus had to be mapped using multiple pointings. We created a mosaic from three individual pointings, with two pointings having an average on-source exposure time of about $160\,$s at both 25 and $37\,\mu$m, and the southernmost pointing only having an on-source exposure time of $35\,$s (due to telescope issues cutting the observation short). Images from each individual pointing were stitched together into a final mosaic using the SOFIA Data Pipeline software REDUX (Clarke et al. 2015).

Flux calibration for all observations were provided by the SOFIA Data Cycle System (DCS) pipeline and the final total photometric errors in the mosaic were derived using the same process described in Paper I. The estimated total photometric errors are 15% for $20\,\mu$m and 10% for $37\,\mu$m. All images then had their astrometry absolutely calibrated using Spitzer-IRAC data by matching up the centroids of point sources in common between the Spitzer and SOFIA data. Absolute astrometry of the final SOFIA images is assumed to be better than $1\rlap{.}''5$. The effective spatial resolution of the data is $\sim 2\rlap{.}''5$ at 20 and $25\,\mu$m and $\sim 3\rlap{.}''2$ at $37\,\mu$m.

In order to perform photometry on mid-infrared point sources, we employed the aperture photometry program *aper. pro*, which is part of the IDL DAOPHOT package available in The IDL Astronomy User's Library (http://idlastro.gsfc.nasa.gov). As was done in Paper I, we measured flux densities for all compact sources and subregions that could be identified in the SOFIA $20\,\mu$m (or $25\,\mu$m) and 37 μm data for Sgr D and W42. We additionally downloaded Spitzer-IRAC (i.e., 3.6, 4.5, 5.8, $8.0\,\mu$m) imaging data and Herschel-PACS (i.e., 70 and $160\,\mu$m) imaging data from their respective online archives and measured fluxes for these same sources at all wavelengths. Tables 1–3 contains the information regarding the position, radius employed for aperture photometry, and background-subtracted flux densities measured at all wavelengths for all of these sources. We employed the same optimal extraction technique as in Paper I to find the optimal aperture to use for photometry. Background subtraction was also performed in the same way as Paper I (i.e., using background statistics from an annulus outside the optimal extraction radius which had the least environmental contamination). For sources in W42, we could not determine source fluxes at $8\,\mu$m due to the Spitzer image being saturated in these areas. For source D in Sgr D, our

Table 1
SOFIA Observational Parameters for Sources in Sgr D and W42

Source	R.A. (J2000)	Decl. (J2000)	20 μm R_{int} ($''$)	20 μm F_{int} (Jy)	20 μm F_{int-bg} (Jy)	25 μm R_{int} ($''$)	25 μm F_{int} (Jy)	25 μm F_{int-bg} (Jy)	37 μm R_{int} ($''$)	37 μm F_{int} (Jy)	37 μm F_{int-bg} (Jy)
Sgr D											
2	17 48 33.92	−28 02 26.7	15	>16.8[a]	>3.93[a]	...	...	...	15	>45.3[a]	>28.4[a]
3	17 48 41.57	−28 08 39.1	54	587	385	...	...	...	54	1571	1460
A	17 48 35.31	−28 00 30.7	19	<6.5[b]	...	...	...	...	19	39.3	23.9
B	17 48 41.51	−28 02 31.3	9	<0.39[b]	...	...	...	...	9	6.47	4.78
C	17 48 43.25	−28 01 46.8	12	15.3	7.99	...	...	...	12	74.1	72.5
D	17 48 48.55	−28 01 11.6	5	2.58	2.56	...	...	...	8	29.2	24.6
W42											
G25.3824	18 38 15.38	−06 47 52.3	...	...	...	8	862.7	797.5	9	1494	1326.6
W42-MME	18 38 14.53	−06 48 02.3	...	...	...	6	305.7	220.5	7	593.5	470.5
1	18 38 15.36	−06 47 40.8	...	...	...	4	62.7	14.7	4	<85.3[b]	...

Notes. R.A. and decl. are for the center of apertures used, not the source peaks. F_{int} indicates total flux inside the aperture. F_{int-bg} is for background-subtracted flux.
[a] Sgr D source 2 is partially off-field in the SOFIA data. The F_{int} and F_{int-bg} values reported are thus lower limits.
[b] Upper limits values given due to non-detection or for sources that are not sufficiently resolved from background emission.

Table 2
Spitzer-IRAC Observational Parameters for Sources in Sgr D and W42

Source	3.6 μm R_{int} ($''$)	3.6 μm F_{int} (Jy)	3.6 μm F_{int-bg} (Jy)	4.5 μm R_{int} ($''$)	4.5 μm F_{int} (Jy)	4.5 μm F_{int-bg} (Jy)	5.8 μm R_{int} ($''$)	5.8 μm F_{int} (Jy)	5.8 μm F_{int-bg} (Jy)	8.0 μm R_{int} ($''$)	8.0 μm F_{int} (Jy)	8.0 μm F_{int-bg} (Jy)
Sgr D												
2	18	0.380	0.212	18	0.407	0.252	21	3.51	2.00	21	8.20	4.89
3	53	4.22	2.16	53	4.54	2.67	53	28.9	15.1	53	78.2	46.7
A	21	0.596	0.276	21	0.522	0.238	24	4.60	1.63	24	11.2	5.48
B	9	<0.051[a]	...	9	<0.060[a]	...	12	0.747	0.293	12	1.64	0.660
C	18	0.529	0.227	18	0.565	0.301	21	3.25	1.51	21	8.18	4.30
D	6	0.095	0.083	6	0.331	0.307	6	0.820	0.658	6	1.23	0.861
W42												
G25.3824	5	1.06	0.738	5	1.27	0.922	7	8.81	5.40	...	sat.	sat.
W42-MME	3	0.23	0.140	4	0.819	0.654	4	3.67	2.46	...	sat.	sat.
1	5	0.22	0.054	4	0.183	0.043	5	1.55	0.364	...	sat.	sat.

Notes. F_{int} indicates total flux inside the aperture. F_{int-bg} is for background-subtracted flux. "sat." means the source is saturated at that wavelength, and thus no accurate flux can be measured.
[a] The F_{int} value is used as the upper limit since the source is difficult to distinguish above the background.

on-source field of view did not cover this source; however, we were chopping east–west, which picked up source D in the eastern chop reference beam, and therefore it shows up as a negative source in our data. Though it is displaced to the west by the distance of the chop throw (180$''$) and negative, accurate photometry could still be performed on the source.

We also used the same methodology set out in Paper I to determine which Spitzer-IRAC data points could be considered nominal data points and which should be considered only upper limits based upon potential contamination from PAH and/or shock-excited H$_2$ emission. As seen in Figure 1, all but two sources are considered *PAH emission dominant* meaning that for those sources we consider their 3.6, 5.8, and 8.0 μm Spitzer data to be upper limits only. As we did in our previous papers, the Herschel 70 and 160 μm data are set to be upper limits for about half of the observations due to the coarser

spatial resolution ($\sim$10$''$) of the data and the high likelihood that the photometry is contaminated by emission from adjacent sources or the extended dusty environments in and around Sgr D and W42.

We set the upper error bar on our photometry as the subtracted background flux value (since background subtraction can be highly variable but never larger than the amount being subtracted), and the lower error bar values for all sources come from the average total photometric error at each wavelength (as discussed in Section 2 and Paper I), which are set to be the estimated photometric errors of 20%, 15%, and 10% for the 4.5, 20/25, and 37 μm bands, respectively. We assume that the photometric errors of the Spitzer-IRAC 3.6, 5.8, and 8.0 μm fluxes are 20% for the sources that are not contaminated by PAH features. The lower error bars of the 70 and 160 μm data points are assumed to be 40% and 30%,
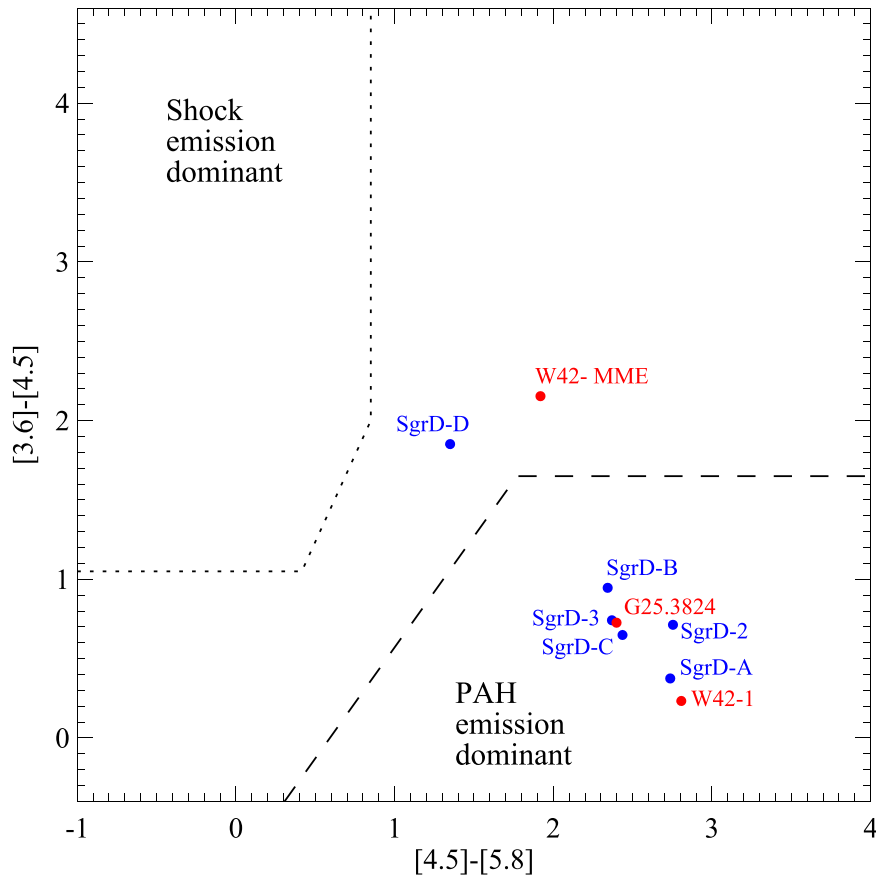
Figure 1. A color–color diagram utilizing the background-subtracted Spitzer-IRAC 3.6, 4.5, and 5.8 μm source photometry to distinguish *shocked emission dominant* and *PAH emission dominant* YSO candidates for the compact sources within Sgr D (blue) and W42 (red). Above (upper left) the dotted line indicates the shock emission dominant regime. Below (bottom right) the dashed line indicates the PAH dominant regime. We adopt this metric from Gutermuth et al. (2009).

respectively, adopting the most conservative (largest) uncertainties of the Herschel compact source catalog (Molinari et al. 2016; Elia et al. 2017).

We used these photometry data to create the near-infrared to far-infrared SEDs of the identified sources and fit them with SED models of MYSOs (a.k.a. "ZT Models;" Zhang & Tan 2011) following the same procedures as described in Paper I. As we did in our previous papers, we used the non-background-subtracted fluxes for the 3.6, 5.8, and 8.0 μm Spitzer-IRAC data in the PAH contaminated sources when fitting the models. We show the ZT MYSO SED model fits as the solid lines (black for the best model fit, and gray for the rest in the group of best-fit models) on top of the derived photometry points for each individual source in Sgr D (Figure 2) and W42 (Figure 3). Table 4 lists the physical properties of the MYSO SED model fits for each source. The observed bolometric luminosities, L_{obs}, of the best-fit models are presented in Column 2 and the true total bolometric luminosities, L_{tot} (i.e., corrected for the foreground extinction and outflow viewing angles), in Column 3. The extinction and the stellar mass of the best models are listed in Columns 4 and 5, respectively. Columns 6 and 7 present the ranges of the foreground extinction and stellar masses derived from the models in the group of best model fits, and the number of best model fits is given in Column 8. Column 9 shows the identification of the individual sources based on the previous studies as well as our criteria of MYSOs and possible MYSOs (pMYSOs) set in Paper I. To summarize, the conditions for a source to be considered an

Table 3
Herschel-PACS Observational Parameters for Sources in Sgr D and W42

Source	70 μm			160 μm		
	R_{int} (″)	F_{int} (Jy)	F_{int-bg} (Jy)	R_{int} (″)	F_{int} (Jy)	F_{int-bg} (Jy)
Sgr D						
2	26	382	241	26	844	157
3	48	3160	2330	64	6230	2695
A	38	685	244	38	<1648[a]	⋯
B	16	97.2	22.7	16	<265[a]	⋯
C	19	<612	UR	19	<733	UR
D	16	163	96.2	16	791	97.2
W42						
G25.3824	13	<2207[a]	⋯	13	<840[a]	⋯
W42-MME	10	<1040[a]	⋯	10	<330[a]	⋯
1	10	<637[a]	⋯	10	<318[a]	⋯

Notes. F_{int} indicates total flux inside the aperture. F_{int-bg} is for background-subtracted flux. "UR" means the source is not sufficiently resolved from the much brighter source 3, and thus flux values can only be considered upper limits.
[a] The F_{int} value is used as the upper limit since the source is difficult to distinguish above the background.

MYSO is that it must (1) have an SED reasonably fit by the MYSO models, (2) have a $M_{star} \geqslant 8\,M_{\odot}$ for the best model fit model, and (3) have $M_{star} \geqslant 8\,M_{\odot}$ for the range of M_{star} of the
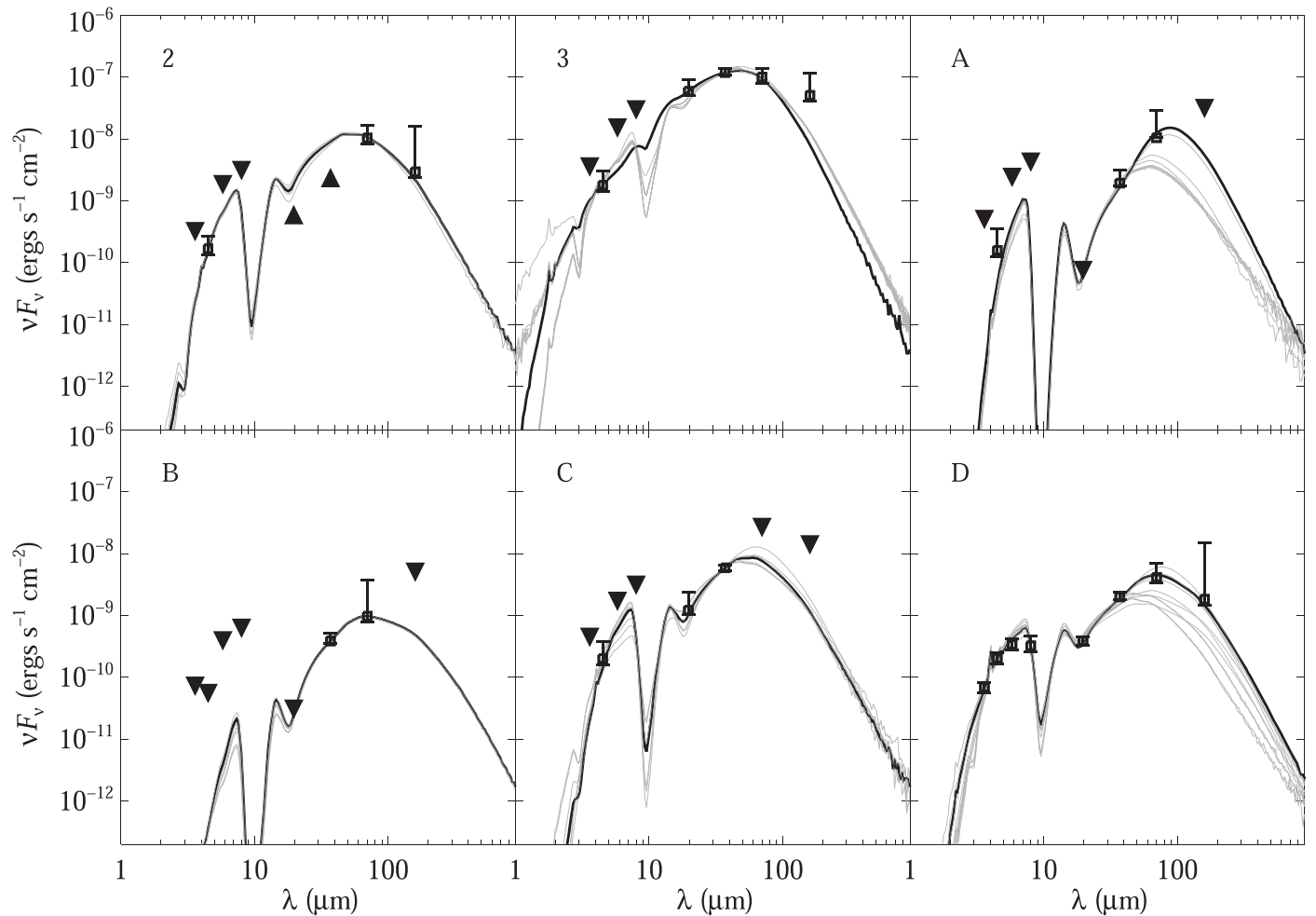
Figure 2. SED fitting with ZT model for compact sources in Sgr D. Black lines are the best-fit model to the SEDs, and the system of gray lines are the remaining fits in the group of best fits (from Table 4). Inverted triangles represent data that are used as upper limits in the SED fits.

group of best-fit models. A pMYSO fulfills only the first two of these criteria.

3. Sgr D

The 6′.6 diameter H II region of Sgr D appears fairly circular in centimeter radio continuum emission (especially at longer radio wavelengths like 18 cm; Rickert et al. 2019) and lies just northwest of a supernova remnant (SNR), G1.05-0.15, which has a similar size (Figure 4). Being a source near the Galactic Center in projection, it was assumed after initial observations (e.g., Kazes & Aubry 1973) to be at a similar distance from the Sun as Sgr A*. More recent observations have argued for distances farther than the Galactic Center (Mehringer et al. 1998) as well as closer (Blum & Damineli 1999). However, using trigonometric parallax measurements of the 22 GHz water maser emission in Sgr D (Sakai et al. 2017), the distance has recently been accurately determined, and indeed has been shown to be a lot closer, situated only 2.36 kpc away. That puts the physical diameter of the H II region at ∼4.5 pc (rather than ∼15 pc), and using the calculations we will discuss later in Section 5.2, reduces the Lyman continuum photon rate of the entire region from $\log N_{LyC} = 50.52$ photon s^{-1} to just $\log N_{LyC} = 49.37$ photon s^{-1}. This is the equivalent to a single O6V star (Panagia 1973), and disqualifies Sgr D from being a GH II based upon its Lyman continuum photon rate.

Looking to the Spitzer-IRAC images and the MSX 22 μm image shown in Conti & Crowther (2004), most of the 6′.6 diameter H II region is not readily apparent in the near and mid-infrared. Even in the Herschel-PACS and SPIRE data, which covers wavelengths with the most infrared emission in the area, the infrared morphology does not resemble the overall radio morphology very well (Figure 4). The fact that most of the radio H II region is not infrared bright could indicate that it may have never been in a giant molecular cloud, or it may be old enough that the molecular cloud around could have dissipated.

Our SOFIA 20 and 37 μm images show the area is dominated in the mid-infrared by a small and bright region (15″ × 40″) on the southeastern side of the larger, circular H II region (Figure 5). The 6 and 18 cm radio continuum observations of Mehringer et al. (1998) show a bright radio peak at this location (named source 3), which they state has the ionizing equivalent of an O5.5 zero-age main-sequence (ZAMS) star. However, they assume a distance to Sgr D of 8.5 kpc, so when we recalculate this using the method in Section 5.2 with the new distance of 2.36 kpc, we derive an ionizing flux equivalent to an O8 ZAMS star ($\log N_{LyC} = 48.36$ photons s^{-1}; Panagia 1973). Mehringer et al. (1998) also identify another compact radio source that lies within the diffuse spherical H II region of Sgr D, which they label source 2 (see Figure 4), which we calculate as having the radio flux equivalent of a B0.5 ZAMS star. We also partially see this
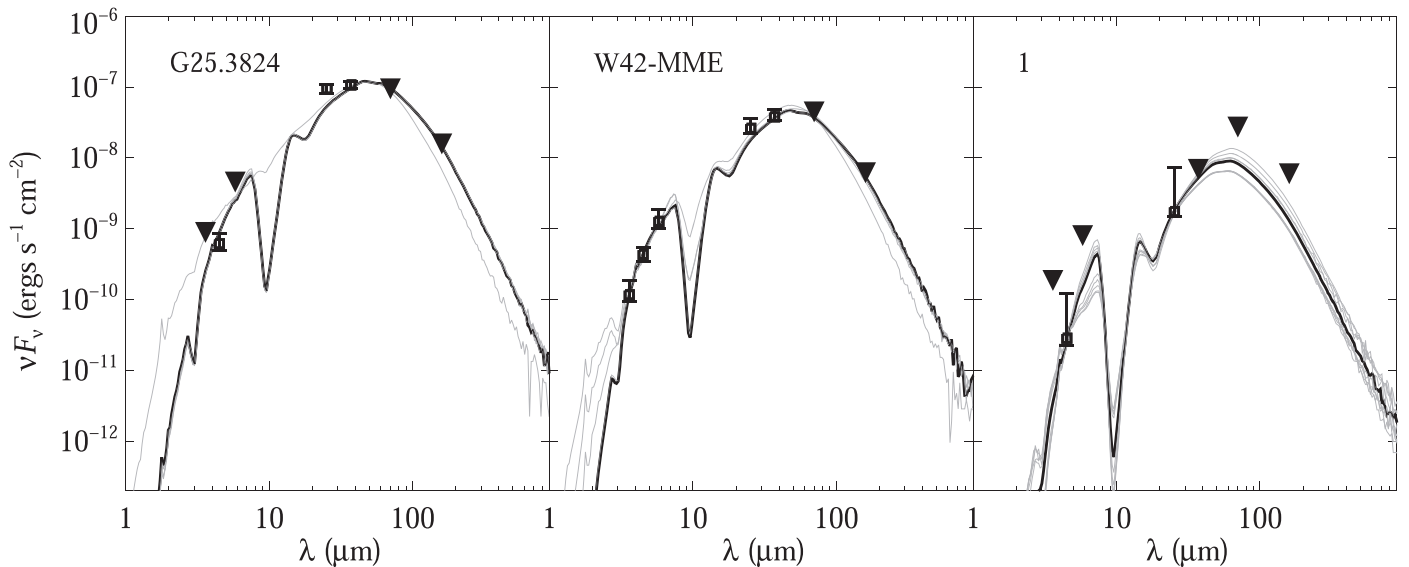
Figure 3. SED fitting with ZT model for compact sources in W42. See Figure 2 for details.

Table 4
SED Fitting Parameters for Sources in Sgr D and W42

Source	L_{obs} $(\times 10^3 L_\odot)$	L_{tot} $(\times 10^3 L_\odot)$	A_v (mag)	M_{star} $(M_\odot)$	A_v Range (mag)			M_{star} Range $(M\odot)$			Best Models	Notes
Sgr D												
2	3.01	10.18	72.1	8.0	55.3	⋯	106.0	8.0	⋯	16.0	5	MYSO
3	33.91	111.64	26.5	16.0	1.7	⋯	32.7	16.0	⋯	32.0	11	MYSO[a]
A	2.74	4.95	264.9	2.0	257.0	⋯	293.0	2.0	⋯	32.0	8	
B	0.24	0.35	76.3	2.0	60.4	⋯	80.5	2.0	⋯	2.0	7	
C	1.98	11.66	92.7	8.0	47.8	⋯	162.0	8.0	⋯	24.0	7	MYSO
D	1.10	1.45	74.2	4.0	58.7	⋯	109.0	2.0	⋯	8.0	11	
W42												
G25.3824	24.54	81.95	40.2	24.0	26.5	⋯	44.4	24.0	⋯	24.0	7	MYSO
W42-MME	9.14	146.68	82.2	32.0	23.8	⋯	82.2	16.0	⋯	32.0	5	MYSO
1	1.63	11.66	98.0	8.0	58.3	⋯	159.0	8.0	⋯	24.0	10	MYSO

Notes. An "MYSO" in the right column denotes an MYSO candidate. An MYSO candidate has values for both M_{star} and its whole M_{star} range greater than 8 $M_\odot$.
[a] No SED fits can be found for Sgr D source 3 that go through the 160 μm data point, indicating a possible excess of a colder environmental dust present.

source on the edge of the field of our SOFIA data (Figure 5). In addition to these two previously identified radio sources, there are four smaller, infrared sources within the larger radio H II region of Sgr D, which we label A–D in order of R.A. in Figure 5.

The elongated infrared structure of radio source 3 has a sharp edge to the southeast, indicating a dense structure present, and infrared source C appears as a fainter region of emission ∼10″ beyond the sharp edge of source 3 to the southeast. Odenwald (1989) suggested that source 3 is a blister type of the H II region seen almost edge-on on the rim of a dark molecular cloud. However, looking to the Herschel 70 μm image of the region shows a dark filament running from this source toward the southeast (Figure 4), and this filament can be seen in emission in the Herschel 250, 350, and 500 μm images. Therefore, source 3 likely formed on the edge of this narrow mid-infrared-dark filament instead of a cloud. In fact, the dark filament runs parallel to the outer contours of the SNR G1.05-0.15 (Figure 4), indicating that either the filament is influencing

the shape of the remnant or that the filament is caused by the sweeping up of material from the expanding SNR. Interestingly, sources 2, 3, and D all lie along a line that meets up with the dark filament to the southwest. This indicates that these sources were likely formed out of that filament, which was perhaps induced by the collision of the Sgr D H II region with the SNR.

In both the SOFIA 20 and 37 μm images the elongated emission of source 3 branches into an X-shape, and curls away from what appears to be a dark lane, which is likely the continuation of the filament. These SOFIA images are reminiscent of an almost edge-on flared disk, where the dark lane separating the brighter and fainter regions of emission is the optically thick torus/disk midplane, and the brighter northwest infrared emission of source 3 curls away from the dark midplane because it is coming from the flared disk surface, and the fainter southeastern emission from source C would be from the other, more obscured side of the disk. Therefore, the infrared emission from sources 3 and C could be
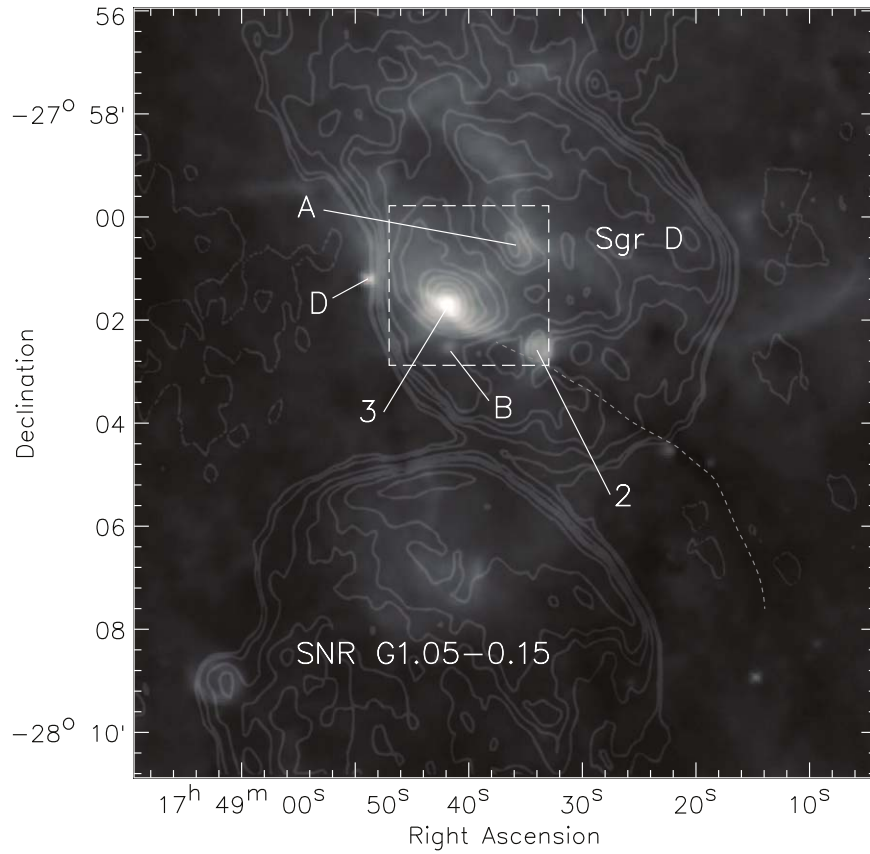
Figure 4. Sgr D and its neighboring SNR G1.05-0.15 as seen by Herschel-PACS at 70 μm overlaid with the 18 cm radio continuum contours of Mehringer et al. (1998). Previously known radio sources 2 and 3 are labeled, as well as infrared sources A, B, and D identified in this work. The white dashed box shows the area covered by the SOFIA observations in Figure 5. The dotted white line delineates a dark filament.
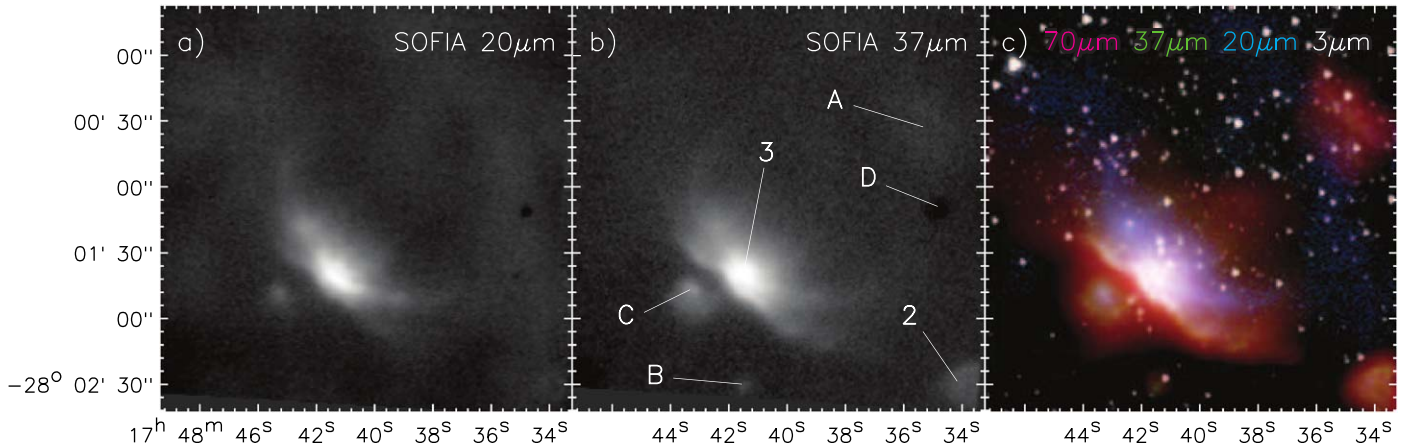

Figure 5. Images of the brightest infrared-emitting sources within the Sgr D radio continuum region at (a) SOFIA 20 μm, and (b) SOFIA 37 μm. Panel (c) illustrates a four-color image of the same region made with Herschel 70 μm (red), SOFIA 37 μm (green), SOFIA 20 μm (blue), and Spitzer 3.6 μm (white; stars) data. Previously known radio sources 2 and 3 are labeled, as well as infrared sources A–D identified in this work. Source D is seen as a negative source, but lies just off the SOFIA field to the east (see Figure 4).

coming from the same ionizing object that resides in a disk within the filament, or the filament is geometrically thin enough that the morphology seen in the infrared mimics that of a disk.

Based upon the ZT model fits to the source SEDs, we find source 3 is likely to be an MYSO with a mass of 16–32 $M_{\odot}$ (Table 4). However, it is the only source that is not well fit by the SED models, since no fit could be found that goes close to or through the Herschel 160 μm data point. As this source is embedded within a larger cold filament, there may be an excess of cold dust in its immediate environment (or seen in projection at our viewing angle) that is not well fit by the core-accretion SED models. That being said, even with SED models that underfit the 160 μm emission, this source appears to be the most massive YSO of all the Sgr D sources identified in the SOFIA data. The range of infrared-derived mass would be the equivalent of a B0.5-O7 ZAMS star (Blum et al. 2000), which

at the maximum extent of this range is consistent with the previously mentioned spectral type of an O8 ZAMS star derived from the radio data.

Source A is near the center of the 6′.6 diameter H II region and it is associated with a weak centimeter radio peak (Figure 4). This source is a very weak and diffuse patch of emission in the mid-infrared with no real discernible peak, and not extremely prominent even in the Herschel 70 μm data. Our best-fit SED to the infrared data yield an estimated stellar mass of only 2.0 $M_\odot$. There is a considerable drop in goodness of fit (as can be seen in Figure 2 with several models underfitting the 70 μm data point), and those models have masses as high as 32 $M_\odot$. Given the best-fit model is of a low-mass star, we do not consider this source an MYSO.

Source B is not seen in the SOFIA 20 μm images and is faint in the Spitzer-IRAC images (Figure 5), but can be seen clearly in the Herschel 70 μm image (Figure 4). Our SED modeling of this source shows it to be a low-mass YSO of 2 $M_\odot$; however, six of the nine data points being fit are upper limits, and thus the model fitting is not well constrained.

As stated earlier, although source C might be emission associated with source 3, we modeled it as an independent source in the event that it indeed is. It is faint in the SOFIA 20 μm image and is brighter and more extended in the SOFIA 37 μm image (Figure 5). It is seen as a peakless but relatively bright emission region extended off of source 3 in the Herschel 70 μm image. Our SED modeling shows that, if it indeed is an independent source, it would be an MYSO candidate with a derived mass of 8 $M_\odot$.

The location of source D is best seen in the Herschel 70 μm data in Figure 4, where it appears as a bright point source. As stated in Section 2, source D was not on the field of our SOFIA data; however, we were chopping east–west and source D was in our eastern chop reference beam, and therefore shows up as a negative source in our data shown in Figure 5. Our SED modeling shows it to be an intermediate-mass YSO with a best-fit mass of 4 $M_\odot$, though model fits do go as high as 8 $M_\odot$.

Though source 2 lies partially off the SOFIA field at 20 and 37 μm, we derived SED fits for the Spitzer and Herschel data for the source and used the SOFIA photometry of the partially seen source as lower limits. This yielded mass estimates of 16–32 $M_\odot$ for the source. This range is consistent with the radio-derived mass estimate of $\sim$16 $M_\odot$ (i.e., a B0.5 ZAMS star).

In summary, the majority of the 6′.6 diameter radio-emitting region of Sgr D does not have any significant infrared emission and thus appears to be the location of only a low level of newly forming stars. Our SED modeling of the infrared sources in that the star formation in the region is dominated by one source, the 16 $M_\odot$ source 3, and that there are likely two (and no more than four) other MYSOs present. Based upon these results, it seems that this region is predominantly powered by a single source (source 3) but, as we will discuss in more detail in Section 6, this source is of relatively modest size compared to the sources powering the GH II regions previously studied in our survey.

4. W42

W42, also known as G25.38−0.18, has centimeter radio continuum emission that is described as having a core-halo structure with a diameter of $\sim$3′ (Garay et al. 1993). Observations in ^{13}CO toward W42 show a line velocity of 58–69 km s^{-1} (e.g., Anderson & Bania 2009; Ai et al. 2013), leading to a near kinematic distance of $\sim$3.7 kpc and a far

distance of $\sim$11.2 kpc. The far kinematic distance was assumed by Conti & Crowther (2004). However, Blum et al. (2000) were able to fit the near-infrared spectra of the brightest star near the center of W42 (labeled as W42 #1) with a ZAMS O5-O6.5 spectral type, which led them to the derivation of a spectrophotometric distance of $\sim$2.2 kpc. Further evidence that this closer value is more accurate comes from Binder & Povich (2018), who adopt this 2.2 kpc value because even the near kinematic value of $\sim$3.7 kpc would make their measured luminosity for the region inconsistent with the cataloged massive stellar population. Blum et al. (2000) provided no error on their 2.2 kpc value but state that the uncertainty in the distance estimate is dominated by the luminosity class assumed and the scatter in the intrinsic brightness of the O stars. They do, however, quote a distance of $2.6^{+1.0}_{-0.7}$ kpc using such errors under the assumption that the stars are main-sequence dwarf stars, and $3.4^{+1.2}_{-0.9}$ kpc for main-sequence giant stars. The assumption of a ZAMS type is more reasonable, and assuming a comparable level of errors for ZAMS stars (i.e., +37% and −27%), we will assume a distance and errors of $2.2^{+0.8}_{-0.6}$ kpc in this work. Moisés et al. (2011) also derived distances to W42 spectrophotometrically and got a value of 2.67 ± 1.40 kpc, which is consistent with the Blum et al. (2000) value and our assumed errors. At this new distance, the derived $\log N_{\mathrm{LyC}}$ value for the entire W42 H II region is 49.44 photons s^{-1} (see Section 5.2), which for comparison is 79% the value for Orion. This value is consistent with the Lyman continuum photon rate of a single $\sim$44 $M_\odot$ O5.5 ZAMS star (Panagia 1973), and thus the centrally located star W42 #1 found by Blum et al. (2000) is thought to be almost fully responsible for ionizing the entire W42 H II region.

The MSX 22 μm image shown in Conti & Crowther (2004) displays two sources, with the brighter, more extended source to the southeast being W42, and the second to the northwest is a source called G25.4NW. While G25.4NW also displays centimeter continuum radio emission and is only 2′.6 from the peak of W42, ^{13}CO line profiles show that it is at a very different velocity from W42 (e.g., Ai et al. 2013), and thus the two sources lie at different distances and are not physically associated. In our SOFIA data we do see both the W42 H II region and G25.4NW at both 25 and 37 μm (Figure 6); however, we will not discuss G25.4NW any further here.

Looking at the large-scale structure of the region, the MSX 22 μm image of W42 (Conti & Crowther 2004) reveals a source with a bright central region with extended emission elongated ($\sim$3′) north–south. Spitzer-IRAC images of W42 revealed fainter dust emission extending perpendicular to, and extending much farther ($r \sim 5′$) than what was seen by MSX. Dewangan et al. (2015a) believe that this fainter emission shows a bipolar structure, roughly east–west, with the brighter, centrally located, north–south elongated infrared emission being central to the waist of the overall bipolar structure. Our SOFIA observations at 25 and 37 μm only detect the extended emission of W42 out to about the same extent as that seen in the MSX 22 μm image (Figure 6), however, with much better resolution ($\sim$3″ versus $\sim$18″).

On smaller scales, looking to the SOFIA images, we find the central region of W42 contains multiple peaks (Figure 7). The brightest peak in the 25 and 37 μm data corresponds to a UCH II region named G025.3824-00.1812 (labeled "G25.3824," for short, in Table 4 and Figures 1 and 3) resolved by the 5 GHz (6 cm) CORNISH Survey (Purcell et al. 2013). This also
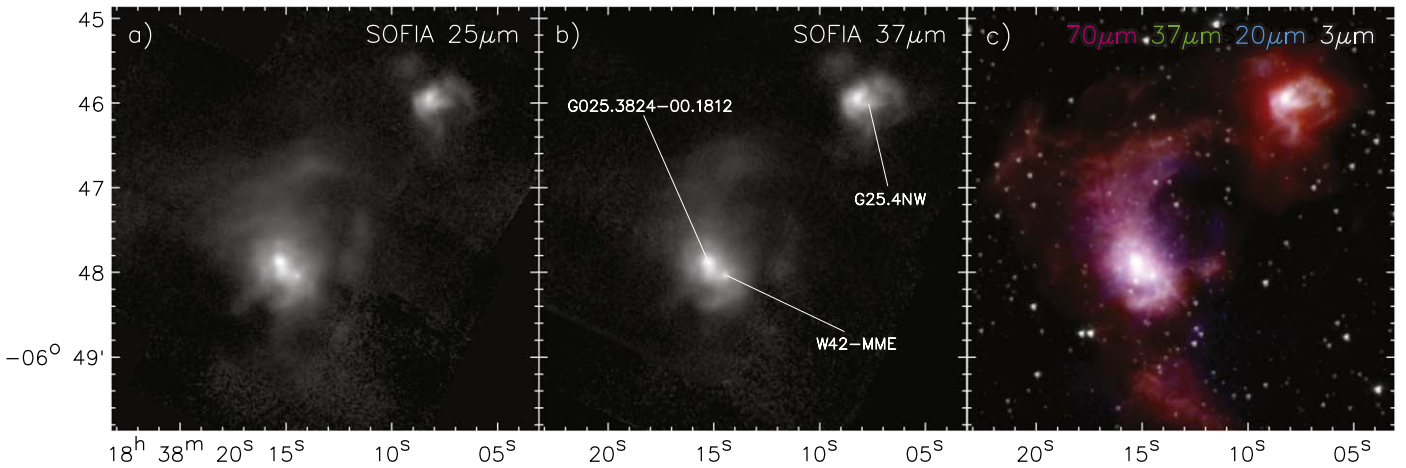
Figure 6. SOFIA images of W42 and G25.4NW at (a) SOFIA 25 μm and (b) SOFIA 37 μm. Panel (c) is a four-color image of the same region made with Herschel 70 μm (red), SOFIA 37 μm (green), SOFIA 25 μm (blue), and Spitzer 3.6 μm (white; stars) data. G25.4NW lies at a different distance than the rest of W42 and is thus not related. The two brightest peaks seen in the mid-infrared are labeled and coincident with the compact radio source G025.3824-00.1812 and the methanol maser source W42-MME.
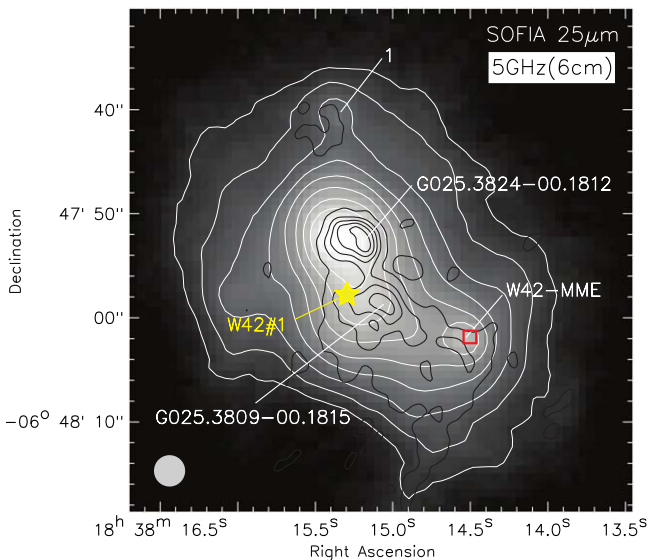

Figure 7. The inner area of W42. The grayscale image and white contours are the SOFIA 25 μm data overlaid with the 5 GHz (6 cm) radio continuum contours (black) from the CORNISH survey (Purcell et al. 2013). Radio sources G025.3824-00.1812 and G025.3809-00.1815 are identified, as well as the infrared peak of W42-MME. Newly identified source 1 is also labeled. The yellow star marks the location of the revealed O5-O6.5V star W42 #1. The red square shows the location of the methanol maser emission detected by Szymczak et al. (2012) that is coincident with W42-MME. The gray dot in the lower-left corner gives the angular resolution of the 25 μm image.

methanol maser source (Szymczak et al. 2012). Dewangan et al. (2015b) detect an infrared source here at wavelengths longer than 2.2 μm (it is also prominent in the Spitzer-IRAC images), which they call W42-MME. They classify this source as a deeply embedded massive YSO ($M \sim 14\,M_\odot$), which is driving a parsec-scale H$_2$ outflow. Based upon our SOFIA data and SED models we confirm the nature of this source as being an MYSO, with a best-fit mass of $32\,M_\odot$ and with the lower limit of the mass range of the best-fit models ($16\,M_\odot$; Table 4) being consistent with the previously derived mass estimate.

There is no peak in the dust emission in the SOFIA data at the location of the central O5-O6.5 star, W42 #1, identified by Blum et al. (2000) though the star itself is easily seen in the Spitzer-IRAC images. This, along with the fact that the source was not so deeply embedded as to allow its spectroscopic identification, may indicate that W42 #1 has evolved far enough to have expelled its natal envelope.

There is a region of emission seen by SOFIA extending southwest from G025.3824-00.1812 $\sim 5''$ west of W42 #1 that corresponds to the radio region G025.3809-00.1815 (CORNISH Survey; Purcell et al. 2013). Based on the radio flux ($S_{5\,\mathrm{GHz}} = 460.83$ mJy), we calculate an N_{LyC} for this region alone and find that it is ionized by the equivalent of a single B0V star. It is unclear how much of the radio flux of G025.3824-00.1812 is due to self-luminance or ionization by W42 #1 nearby. This goes for 025.3809-00.1815 as well, given that it too is only $\sim 5''$ away from W42 #1. We cannot isolate the emission from 025.3809-00.1815 well enough to get accurate fluxes for our SED modeling. As for the near-infrared emission associated with W42 #1, Dewangan et al. (2015a) resolve it into three point sources, but do not have sufficient data to classify them individually. One would assume that the brightest of the three objects is likely to be the $\sim 44\,M_\odot$ O5-O6.5 star identified spectroscopically by Blum et al. (2000).

There is one final peak seen in the SOFIA data, most prominent at 25 μm. It is north of G025.3824-00.1812, and is associated with a near-infrared source seen in the Spitzer-IRAC images. We label this source 1 in Figure 7. Its emission cannot be completely separated from the overall extended emission in the SOFIA images, but SED fits to the photometry show that it is also might be an MYSO with a best-fit mass 8 $M_\odot$ (Table 4). The accuracy of the mass and luminosity parameters derived from the

corresponds to the only peak in the extended emission of W42 seen in the Herschel 70 μm image, as well as the brightest peak seen in the Spitzer-IRAC images. Dewangan et al. (2015a) obtained high spatial resolution near-infrared images of this source (0.''027) that resolve the source into five point sources, but they were not able to characterize the sources individually. Based on the radio flux of G025.3824-00.1812 ($S_{5\,\mathrm{GHz}} = 200.13$ mJy; Purcell et al. 2013), we calculate an N_{LyC} for this region alone and find that it is ionized by the equivalent of a single B0.5V star, which would have a mass of $M \sim 16\,M_\odot$. Our infrared-derived mass from the best fits of the SED modeling yields a moderately larger stellar mass of $24\,M_\odot$ (Table 4).

The next brightest peak in the SOFIA data is the southwestern peak that is associated with the location of a 6.7 GHz

SED fits for all of these sources is likely to be uncertain due to the unknown contribution of the heating of the dust by the revealed O-star W42 #1. This also goes for the radio-derived masses of these sources, since W42 #1 is thought to be responsible for ionizing the entirety of the large-scale H II emission of W42.

In summary, the total radio continuum flux from W42 is equal to the ionizing power of the observed O5-O6.5V star of Blum et al. (2000), and thus it is likely that this one star, W42 #1, is responsible for most of the radio continuum emission seen in the region. The overall Lyman continuum photon rate from the entire region is less than that of Orion. Though the central $r \sim 1'$ (~0.6 pc) region has several dozen low-mass YSOs (Blum et al. 2000; Dewangan et al. 2015a), the MYSO population is small, consisting of an MYSO associated with W42-MME, a UCH II region G025.3824-00.1812 hosting a young MYSO, a weak radio-emitting MYSO associated with infrared source 1, and potentially another UCH II region G025.3809-00.1815 hosting another MYSO. As we will discuss further in Section 6, this MYSO population is modest when compared to the GH II regions we have previously studied.

5. Reassessing the GH II Region Census

In light of the fact that the new distances for Sgr D and W42 have led to their demotion from GH II region status, we were motivated to perform in-depth literature searches for recent and more accurate distance measurements toward each of the 56 sources in the Conti & Crowther (2004) census. In this section, we will briefly describe the different methods of distance determination, describe the calculation of N_{LyC} performed, and list the sources that do and do not qualify as GH II regions based upon these updated calculations.

5.1. Updating Distance Measurements

An accurate determination of the distance toward each GH II region is critically tied to their identity as a GH II region, since the derived luminosity, and more importantly derived Lyman continuum photon rate, are proportional to the square of their distance from the Sun. From our literature search on each source we compiled the latest and/or most reliable distance estimate for each source. The vast majority of sources have had their accepted distances adjusted since the publications of Conti & Crowther (2004).

In most cases there are several distance estimates, and therefore we chose to adopt the distance derived via the measurements that were most precise. Though measurements made by any particular methodology will have a range of precisions, in general we can rank the methods of determining distance from most accurate to least accurate as (1) trigonometric parallax measurements either via circumstellar masers, or via GAIA measurements of the revealed stellar clusters associated with the ionized region, (2) spectrophotometric measurements, (3) kinematically derived distances outside the solar circle or inside the solar circle but at a tangent point, (4) sources with large differences in their near/far kinematic distance values but for which there is optical or Hα emission (an indication of low interstellar extinction) and thus indicating the near distance; (5) an assumed association of the GH II region with a nearby object/region at similar v_{lsr} and for which a distance is more accurately known (e.g., regions near the Galactic Center, which are assumed to be at the same distance

as Sgr A* derived via maser parallax measurements), (6) kinematically derived distances where sources have measured H I (or other species) absorption line velocity observations that help resolve the kinematic distance ambiguity, and finally, (7) kinematically derived distances with near/far ambiguity but no supporting deconflicting observations, or having conflicting observations from methods with similar accuracy, which means the kinematic distance ambiguity cannot be clearly resolved. For more detailed explanations of all of these methods, see the thorough discussion on distance measurements and their accuracies in Urquhart et al. (2018).

Since there are a variety of Galactic rotation curve models, if our literature search only turned up kinematic distance measurements for a source, we recorded the v_{lsr} values from line measurements (typically radio Hα lines) that had the best reported precision. We then derived kinematic distances ourselves so that all sources have kinematic distance determinations performed in a consistent way. For this we chose to apply the Monte Carlo kinematic distance method of Wenger et al. (2018), which utilizes the Reid et al. (2014) rotation curve and updated solar motion parameters (the most important parameter of which to point out is the assumed distance to the Galactic Center of $R_0 = 8.34 \pm 0.16$ kpc).

Table 5 lists the old distances (Column 4) from Conti & Crowther (2004) along with the newly adopted distances with their associated errors (Column 5), the reference for the new distance measurement and error (Column 6), and which of the methodologies listed above was employed in the distance measurement (Column 7). For sources with only kinematic distance determinations, Table 6 lists the adopted v_{lsr} value from the literature, our calculated near/far (or tangent) distances found via the Monte Carlo kinematic distance method, and the method used to achieve a kinematic distance ambiguity resolution (KDAR) to get the adopted distance listed in Table 5. The Appendix provides an in-depth discussion of the distance measurements toward each source, and the reasoning behind the adopted distances tabulated in Table 5.

5.2. Recalculating Lyman Continuum Photon Rate

Once new distance measurements toward all sources were obtained, we recalculated the Lyman continuum photon rate of each source. We used the relationship for the observed Lyman continuum photon rate, N'_{LyC}, defined in Mezger et al. (1974):

$$N'_{LyC} = 4.761 \times 10^{48} a(\nu, T_e)^{-1} \left(\frac{\nu}{GHz}\right)^{0.1}$$
$$\times \left(\frac{T_e}{K}\right)^{-0.45} \left(\frac{S_\nu}{Jy}\right) \left(\frac{d}{kpc}\right)^2 \text{ photons s}^{-1}, \quad (1)$$

where ν is frequency, T_e is electron temperature, S_ν is radio flux density, and d is the distance to the source. The $a(\nu, T_e)$ term is approximately equal to 1, but we directly calculate it from the electron temperature through the expression given by Mezger & Henderson (1967):

$$a(\nu, T_e) = 0.366 \left(\frac{\nu}{GHz}\right)^{0.1} \left(\frac{T_e}{K}\right)^{-0.15}$$
$$\times \left\{\ln\left(4.995 \times 10^{-2} \left(\frac{\nu}{GHz}\right)^{-1}\right) + 1.5 \ln\left(\frac{T_e}{K}\right)\right\}.$$
$$(2)$$

Table 5
Updated List of Assumed GH II Region Properties

(1) Name	(2) ℓ (°)	(3) b (°)	(4) Old d (kpc)	(5) New d (kpc)	(6) Ref.	(7) Meth.	(8) $S_{6\,cm}$ (Jy)	(9) $\theta_{6\,cm}$ (′)	(10) T_e (K)	(11) Ref. (K)
G0.361-0.780	0.361	−0.780	8.0	$8.23^{+0.20}_{-0.17}$	DWB80	Kin	7.4 ± 0.7	5.2 ± 0.4	5100 ± 2500	DWB80
G0.394-0.540	0.394	−0.540	8.0	$8.23^{+0.18}_{-0.15}$	DWB80	Kin	8.8 ± 0.9	5.6 ± 0.4	7500 ± 2500	DWB80
G0.489-0.668	0.489	−0.668	8.0	$8.25^{+0.25}_{-0.33}$	DWB80	Kin	8.4 ± 0.8	3.7 ± 0.3	5500 ± 2500	DWB80
Sgr B1	0.518	−0.065	8.0	$7.80^{+0.80}_{-0.70}$	RMZ09	Sgr B2[a]	35.1 ± 3.5	3.7 ± 0.3	7200 ± 2000	DWB80
G0.572-0.628	0.572	−0.628	8	$8.18^{+0.25}_{-0.18}$	DWB80	Kin	7.2 ± 0.7	2.5 ± 0.2	6200 ± 2500	DWB80
Sgr D	1.149	−0.062	8.0	$2.36^{+0.58}_{-0.39}$	SON17	Mpara	19.3 ± 1.9	5.5 ± 0.4	5000 ± 500	WWB83
G2.303+0.243	2.303	0.243	14.3	$13.48^{+0.98}_{-0.76}$	L89	Kin	7.3 ± 0.7	5.9 ± 0.5	3700 ± 2500	DWB80
G3.270-0.101	3.270	−0.101	14.3	$14.33^{+0.76}_{-0.82}$	JDD13	Kin	9.9 ± 1.0	5.7 ± 0.4	7440 ± 280	WBA19
G4.412+0.118	4.412	0.118	14.6	$14.97^{+0.77}_{-0.58}$	RWJ16	Kin	10.4 ± 1.0	4.9 ± 0.4	5700 ± 2500	DWB80
M8	5.973	−1.178	2.8	1.34 ± 0.07	RPB20	Gpara	113.4 ± 11.3	7.5 ± 0.6	8180 ± 70	WBA19
G8.137+0.228	8.137	0.228	13.5	$3.38^{+0.28}_{-0.36}$	QRB06	Kin	8.2 ± 0.8	1.8 ± 0.1	7090 ± 60	WBA19
W31-South	10.159	−0.349	4.5	3.40 ± 0.3	RDC01	Spec	66.3 ± 6.6	2.9 ± 0.2	6830 ± 30	WBA19
W31-North	10.315	−0.150	15.0	1.75 ± 0.25	DZS15	Spec	20.5 ± 2.1	3.1 ± 0.2	6800 ± 40	WBA19
M17	15.032	−0.687	2.4	$1.98^{+0.14}_{-0.12}$	XMR11	Mpara	844.5 ± 84.5	4.5 ± 0.3	9280 ± 120	WBA19
G20.733-0.087	20.733	−0.087	11.8	$11.69^{+0.34}_{-0.44}$	QRB06	Kin	19.5 ± 2.0	6.1 ± 0.5	5590 ± 90	WBA19
W42	25.382	−0.177	11.5	$2.20^{+0.80}_{-0.60}$	BCD00	Spec	29.5 ± 3.0	3.7 ± 0.3	7460 ± 70	WBA19
G29.944-0.042	29.944	−0.042	6.2	$5.71^{+0.50}_{-0.42}$	ZMS14	Mpara	25.5 ± 2.6	3.7 ± 0.3	6510 ± 90	WBA19
W43	30.776	−0.029	6.2	$5.49^{+0.39}_{-0.34}$	ZMS14	Mpara	62.2 ± 6.2	4.1 ± 0.3	6567 ± 30	WBA19
G32.80+0.19	32.797	0.192	12.9	$12.85^{+0.44}_{-0.34}$	QRB06	Kin	5.8 ± 0.6	2.3 ± 0.2	8625 ± 49	WBA19
W49A	43.169	0.002	11.8	$11.11^{+0.79}_{-0.69}$	ZRM13	Mpara	69.0 ± 6.9	3.0 ± 0.2	7876 ± 35	WBA19
G48.596+0.042	48.596	0.042	9.8	$10.75^{+0.61}_{-0.55}$	ZRM13	Mpara	12.2 ± 1.5	4.2 ± 0.3	7800 ± 2500	DWB80
G48.9-0.3	48.930	−0.286	5.5	$5.62^{+0.59}_{-0.49}$	NKO15	Mpara	24.3 ± 2.9	4.4 ± 0.3	8440 ± 60	WBA19
W51A:G49.4-0.3	49.384	−0.298	5.5	$5.41^{+0.31}_{-0.28}$	SRB10	Mpara	27.2 ± 3.3	2.8 ± 0.2	8585 ± 65	WBA19
W51A:G49.5-0.4	49.486	−0.381	5.5	$5.41^{+0.31}_{-0.28}$	SRB10	Mpara	110.4 ± 13.2	2.8 ± 0.2	7166 ± 25	WBA19
K3-50(W58A)	70.300	1.600	8.6	$7.64^{+0.81}_{-0.54}$	QRB06	KOG	13.0 ± 1.6	2.1 ± 0.2	10810 ± 130	WBA19
DR7	79.293	1.296	8.3	$7.30^{+0.84}_{-0.72}$	QRB06	KOG	15.8 ± 1.9	3.4 ± 0.3	8693 ± 86	WBA19
W3	133.720	1.210	4.2	$2.30^{+0.19}_{-0.16}$	NGD19	Gpara	74.7 ± 9.0	3.4 ± 0.3	8977 ± 38	WBA19
RCW 42	274.013	−1.141	6.4	$5.97^{+0.90}_{-0.72}$	CH87	KOG	39.9 ± 4.0	2.9 ± 0.2	7900^{+400}_{-400}	CH87
RCW 46	282.023	−1.180	5.9	$5.77^{+0.77}_{-0.77}$	CH87	KOG	40.9 ± 4.1	3.8 ± 0.3	6200^{+300}_{-400}	CH87
RCW 49	284.301	−0.344	4.7	4.16 ± 0.27	VKB13	Spec	263.2 ± 26.3	7.4 ± 0.6	8000^{+300}_{-300}	CH87
NGC 3372	287.379	−0.629	2.5	2.3 ± 0.1	S06	η Car[a]	145.6 ± 14.6	7.0 ± 0.5	7200^{+400}_{-500}	CH87
G289.066-0.357	289.066	−0.357	7.9	$7.15^{+0.54}_{-0.93}$	CH87	KOG	16.4 ± 1.6	6.0 ± 0.5	8500^{+600}_{-700}	CH87
NGC 3576	291.284	−0.712	3.1	2.77 ± 0.31	BP18	Gpara	113.0 ± 11.3	2.5 ± 0.2	7500^{+400}_{-400}	CH87
NGC 3603	291.610	−0.528	7.9	7.20 ± 0.10	DMW19	Gpara	261.0 ± 26.1	6.9 ± 0.5	6900^{+100}_{-100}	CH87
G298.227-0.340	298.227	−0.340	10.4	12.4 ± 1.7	DNB16	Spec	47.4 ± 4.7	3.8 ± 0.3	8600^{+600}_{-700}	CH87
G298.862-0.438	298.862	−0.438	10.4	12.4 ± 1.7	DNB16	Spec	42.4 ± 4.2	3.8 ± 0.3	6600^{+100}_{-100}	CH87
G305.359+0.194	305.359	0.194	3.5	3.59 ± 0.85	BP18	Gpara	56.4 ± 5.6	3.5 ± 0.3	5100^{+200}_{-300}	CH87
G319.158-0.398	319.158	−0.398	11.5	$11.26^{+0.35}_{-0.42}$	CH87	Kin	11.2 ± 1.1	5.9 ± 0.5	6300^{+400}_{-400}	CH87
G319.392-0.009	319.392	−0.009	11.5	$11.78^{+0.34}_{-0.42}$	CH87	Kin	8.9 ± 0.9	3.5 ± 0.3	7700^{+1000}_{-1300}	CH87
G320.327-0.184	320.327	−0.184	12.6	$0.64^{+0.38}_{-0.27}$	CH87	Kin	6.3 ± 0.6	5.0 ± 0.4	5700^{+400}_{-400}	CH87
RCW 97	327.304	−0.552	3.0	$2.98^{+0.23}_{-0.36}$	WMS06	Kin	64.9 ± 6.5	2.9 ± 0.2	4700^{+300}_{-400}	CH87
G327.993-0.100	327.993	−0.100	11.4	$2.80^{+0.31}_{-0.31}$	CH87	Kin	5.9 ± 0.6	2.7 ± 0.2	6000^{+600}_{-700}	CH87
G330.868-0.365	330.868	−0.365	10.8	$3.44^{+0.47}_{-0.36}$	CH87	Kin	14.7 ± 1.5	4.0 ± 0.3	4900^{+400}_{-500}	CH87
G331.324-0.348	331.324	−0.348	10.8	3.29 ± 0.58	PAC12	Spec	6.5 ± 0.7	1.8 ± 0.1	3500^{+200}_{-200}	CH87
G331.354+1.072	331.354	1.072	10.8	$4.50^{+0.55}_{-0.34}$	CH87	Kin	6.7 ± 0.7	4.9 ± 0.4	5400^{+400}_{-400}	CH87
G331.529-0.084	331.529	−0.084	10.8	7.31 ± 2.19	CH87	Kin	47.1 ± 4.7	4.0 ± 0.3	6200^{+400}_{-400}	CH87
G333.122-0.446	333.122	−0.446	3.5	2.60 ± 0.20	FBD05	Spec	49.5 ± 5.0	4.5 ± 0.3	5800^{+500}_{-600}	CH87
G333.293-0.382	333.293	−0.382	3.5	2.60 ± 0.70	RAO09	Spec	45.5 ± 4.6	3.8 ± 0.3	6300^{+300}_{-400}	CH87
G333.610-0.217	333.610	−0.217	3.1	2.54 ± 0.71	RPB20	Gpara	116.2 ± 11.6	3.7 ± 0.3	6200^{+200}_{-300}	CH87
G338.398+0.164	338.398	0.164	13.1	$13.29^{+0.25}_{-0.45}$	CH87	Kin	25.7 ± 2.6	5.5 ± 0.4	6600^{+400}_{-400}	CH87
G338.400-0.201	338.400	−0.201	15.7	$15.71^{+0.58}_{-0.40}$	CH87	KOG	6.3 ± 0.6	3.3 ± 0.3	9100^{+700}_{-400}	CH87
G345.555-0.043	345.555	−0.043	15.2	$15.28^{+0.57}_{-0.35}$	CH87	Kin	15.1 ± 1.5	5.5 ± 0.4	6500^{+400}_{-400}	CH87
G345.645+0.009	345.645	0.009	15.2	$14.97^{+0.39}_{-0.45}$	CH87	Kin	11.2 ± 1.1	4.2 ± 0.3	7800^{+500}_{-500}	CH87
G347.611+0.204	347.611	0.204	6.6	7.90 ± 0.8	BGH12	Spec	23.2 ± 2.3	6.1 ± 0.5	4000^{+300}_{-400}	CH87

Table 5
(Continued)

(1) Name	(2) ℓ (°)	(3) b (°)	(4) Old d (kpc)	(5) New d (kpc)	(6) Ref.	(7) Meth.	(8) $S_{6\,cm}$ (Jy)	(9) $\theta_{6\,cm}$ (′)	(10) T_e	(11) Ref. (K)
G351.467-0.462	351.467	−0.462	13.7	$3.24^{+0.34}_{-0.26}$	CH87	Spec[a]	4.7 ± 0.5	2.7 ± 0.2	7460 ± 120	WBA19
Sgr C	359.429	−0.090	8.0	$8.34^{+0.15}_{-0.17}$	CH87	Tang	19.3 ± 1.9	4.3 ± 0.3	9300^{+500}_{-500}	CH87

Notes. References in Column 6 are for distance measurements, and Column 11 are for the electron temperature measurements, and use the following abbreviations: BCD00 (Blum et al. 2000), BDC01 (Blum et al. 2001), BGH12 (Borissova et al. 2012), BP18 (Binder & Povich 2018), CH87 (Caswell & Haynes 1987), DMW19 (Drew et al. 2019), DNB16 (de la Fuente et al. 2016), DWB80 (Downes et al. 1980), DZS15 (Deharveng et al. 2015), FBD05 (Figuerêdo et al. 2005), JDD13 (Jones et al. 2013), L89 (Lockman 1989), NGD19 (Navarete et al. 2019), NKO15 (Nagayama et al. 2015), PAC12 (Pinheiro et al. 2012), QRB06 (Quireza et al. 2006), RAO09 (Roman-Lopes et al. 2009), RMZ09 (Reid et al. 2009), RPB20 (Ramírez-Tannus et al. 2020), RWJ16 (Rathborne et al. 2016), S06 (Smith 2006), SON17 (Sakai et al. 2017), SRB10 (Sato et al. 2010), VKB13 (Vargas Álvarez et al. 2013), WBA19 (Wenger et al. 2019), WMS06 (Wyrowski et al. 2006), WWB83 (Wink et al. 1983), XMR11 (Xu et al. 2011), ZMS14 (Zhang et al. 2014), and ZRM13 (Zhang et al. 2013). Column 7: The methods used for determining distances are "Mpara/Gpara"—maser/GAIA parallax; "Spec"—Spectrophotometric/Photometric; "Kin"—Kinematic distance with a resolved distance ambiguity (see Table 6 for more details); "KOG/Tang"—Kinematic distance with no ambiguity because it resides in the outer Galaxy or at a tangent point; "Sgr B2"—assumed to be at the maser parallax-derived distance of Sgr B2, "η Car"—assumed to be at the distance of η Car.
[a] Distance derived spectrophotometrically by Borissova et al. (2006), without quoting a formal uncertainty. The spectrophotometric value is the same as the kinematically derived value, so we quote the kinematic distance with its formal error.

Table 6
Parameters Used in Determining Distances to Sources That Only Have Kinematic Information

Name	v_{lsr} (km s^{-1})	v_{lsr} References	Near Distance	Far Distance	KDAR	KDAR Method	KDAR References
G0.361-0.780	20.0 ± 5.0	Downes et al. (1980)	$8.23^{+0.20}_{-0.17}$	$8.45^{+0.15}_{-0.25}$	Near	Hα	Russeil (2003)
G0.394-0.540	24.0 ± 5.0	Downes et al. (1980)	$8.23^{+0.18}_{-0.15}$	$8.30^{+0.23}_{-0.12}$	Near	Hα	Russeil (2003)
G0.489-0.668	17.0 ± 5.0	Downes et al. (1980)	$8.25^{+0.25}_{-0.33}$	$8.44^{+0.33}_{-0.17}$	Near	Hα	Russeil (2003)
G0.572-0.628	20.0 ± 5.0	Downes et al. (1980)	$8.18^{+0.25}_{-0.18}$	$8.48^{+0.20}_{-0.20}$	Near	Hα	Russeil (2003)
G2.303+0.243	4.9 ± 0.7	Lockman (1989)	$3.14^{+0.74}_{-0.89}$	$13.48^{+0.98}_{-0.76}$	Far	OH	Russeil (2003)
G3.270-0.101	4.9 ± 0.8	Caswell & Haynes (1987)	$2.45^{+0.56}_{-0.81}$	$14.33^{+0.76}_{-0.82}$	Far	H I	Jones et al. (2013)
G4.412+0.118	4.23 ± 0.25	Rathborne et al. (2016)	$1.79^{+0.43}_{-0.75}$	$14.97^{+0.77}_{-0.58}$	Far	H I	Jones et al. (2013)
G8.137+0.228	20.31 ± 0.06	Quireza et al. (2006)	$3.38^{+0.28}_{-0.36}$	$13.17^{+0.44}_{-0.39}$	Near	H I	Jones et al. (2013)
G20.733-0.087	55.96 ± 0.04	Quireza et al. (2006)	$3.85^{+0.39}_{-0.27}$	$11.69^{+0.34}_{-0.44}$	Far	H I	Urquhart et al. (2018)
G32.80+0.19	15.46 ± 0.15	Quireza et al. (2006)	$1.10^{+0.25}_{-0.33}$	$12.85^{+0.44}_{-0.34}$	Far	Masers[a]	Zhang et al. (2019)
G319.158-0.398	21.0 ± 1.0	Caswell & Haynes (1987)	$1.41^{+0.21}_{-0.40}$	$11.26^{+0.35}_{-0.42}$	Far	H I	Urquhart et al. (2012)
G319.392-0.009	−14.0 ± 1.0	Caswell & Haynes (1987)	$1.01^{+0.23}_{-0.43}$	$11.78^{+0.34}_{-0.42}$	Far	H I	Urquhart et al. (2012)
G320.327-0.184	−11.0 ± 1.0	Caswell & Haynes (1987)	$0.64^{+0.38}_{-0.27}$	$12.02^{+0.54}_{-0.30}$	Near?[b]	H I[b]	Urquhart et al. (2018)
RCW 97	−47.5 ± 0.1	Wyrowski et al. (2006)	$2.98^{+0.23}_{-0.36}$	$11.14^{+0.34}_{-0.41}$	Near	H I	Urquhart et al. (2012)
G327.993-0.100	−45.0 ± 1.0	Caswell & Haynes (1987)	$2.80^{+0.31}_{-0.31}$	$11.28^{+0.38}_{-0.36}$	Near	H I	Urquhart et al. (2018)
G330.868-0.365	−56.0 ± 1.0	Caswell & Haynes (1987)	$3.44^{+0.47}_{-0.36}$	$11.02^{+0.47}_{-0.36}$	Near	Optical	Paladini et al. (2004)
G331.354+1.072	−79.0 ± 1.0	Caswell & Haynes (1987)	$4.50^{+0.55}_{-0.34}$	$9.98^{+0.46}_{-0.46}$	Near	H I	Urquhart et al. (2012)
G331.529-0.084	−89.0 ± 1.0	Caswell & Haynes (1987)	$7.31 ± 2.19^{c}$	…	Tangent?[c]	[c]	Merello et al. (2013)
G338.398+0.164	−29.0 ± 1.0	Caswell & Haynes (1987)	$2.32^{+0.20}_{-0.31}$	$13.29^{+0.25}_{-0.45}$	Far?[b]	H I[b]	Urquhart et al. (2018)
G345.555-0.043	−6.0 ± 1.0	Caswell & Haynes (1987)	$0.60^{+0.44}_{-0.19}$	$15.28^{+0.57}_{-0.35}$	Far	CO/H$_2$CO	Caswell & Haynes (1987)
G345.645+0.009	−10.0 ± 1.0	Caswell & Haynes (1987)	$1.10^{+0.41}_{-0.19}$	$14.97^{+0.39}_{-0.45}$	Far	H I	Urquhart et al. (2012)

Notes. KDAR stands for kinematic distance ambiguity resolution. "Hα"—the presence of Hα emission indicating the near kinematic distance; "OH," "H I," and "CO/H$_2$CO"—the presence of these absorption features indicating near or far distance, and "Optical"—the presence of optical emission from the region indicates near distance.
[a] Low precision maser parallax measurements consistent with the higher precision kinematic far distance.
[b] Conflicting absorption line measurements pointing to both near and far distances.
[c] Conflicting information points to near, far, and tangent distance; therefore, the tangent is quoted with the error that covers both near and far distances.

Where available, we updated the T_e values tabulated by Conti & Crowther (2004) with more precise measurements. All new measurements adopted here come from Wenger et al. (2019), which expands upon, and in some cases updates (with higher quality observations) the work of Balser et al. (2015). These adopted T_e values with their errors are given in Column 10 of

Table 5, and the references for these measurements are given in Column 11.

From here we use the methodology in Smith et al. (1978) to estimate the fraction of photons lost to dust absorption to correct the observed Lyman continuum photon rate, N'_{LyC}, and derive the intrinsic Lyman continuum photon rate, N_{LyC}. This

calculation requires first calculating the galactocentric distance of each source, which we calculated with the assumption that the Sun is 8.34 ± 0.16 kpc from the Galactic Center using the values from Reid et al. (2014), which are the values also used in the calculation adopted for obtaining kinematic distances; this is also different from the work of Conti & Crowther (2004) who used a distance of $R_0 = 8.0$ kpc. We simply use the law of cosines to determine the galactocentric distance to each source:

$$R_{GC} = [d^2 + R_0^2 - 2\,d\,R_0\cos(l)]^{0.5} \text{ kpc}, \qquad (3)$$

where l is the source Galactic longitude. Next, one calculates the helium absorption cross-section parameter, $x\sigma_{He}/x_1\sigma_\nu$, defined and discussed in Smith et al. (1978), which was found to have the following empirically derived relationship with galactocentric distance (see also Churchwell et al. 1978):

$$
\begin{aligned}
&x\sigma_{He}/x_1\sigma_\nu \\
&= \begin{cases} 5.0 - 0.4\,R_{GC}(\pm 2.0), & \text{for } R_{GC} < 10 \text{ kpc} \\ 1.0(\pm 1.0), & \text{for } R_{GC} > 10 \text{ kpc}. \end{cases}
\end{aligned} \qquad (4)
$$

Calculation of intrinsic Lyman continuum photon rate further requires the calculation of the electron density of the source, N_e, which we adopted from Schraml & Mezger (1969):

$$N_e = 98.152\,a(\nu, T_e)^{-0.5}\left(\frac{\nu}{\text{GHz}}\right)^{0.05}\left(\frac{T_e}{\text{K}}\right)^{0.175}$$

$$\times \left(\frac{S_\nu}{\text{Jy}}\right)^{0.5}\left(\frac{d}{\text{kpc}}\right)^{-0.5}\left(\frac{\theta}{\text{arcmin}}\right)^{-1.5} \text{ cm}^{-3}, \qquad (5)$$

where θ is the half-power width of a Gaussian fit to the radio source.

Using the resultant values derived for N'_{LyC} from Equation (1), N_e from Equation (5), and $x\sigma_{He}/x_1\sigma_\nu$ from Equation (4), we plug those values into the equation for H-photon absorption optical depth given by Smith et al. (1978):

$$\tau_H = 3.4 \times 10^{-18}(N'_{LyC}\,N_e)^{1/3}\,a_o^{-1}(x\sigma_{He}/x_1\sigma_\nu), \qquad (6)$$

where a_o is the ratio of the absorption cross sections for He-photons and H-photons. We use the assumption from Smith et al. (1978) and assume a value to 6.0 ± 1.0.

Smith et al. (1978) provide a table of values for the fraction of Lyman continuum photons absorbed by the gas, f_{net}, and their corresponding values of τ_H (as well as other parameters). We fit these data in the table with a functional form, given by the equation:

$$f_{net} = -0.234\ln(\tau_H) + 0.259. \qquad (7)$$

This equation reproduces the f_{net} values for the GH II regions tabulated in Smith et al. (1978) to within 6% (using only the parameters from that work). Finally, we calculate the intrinsic Lyman continuum photon rate using

$$N_{LyC} = N'_{LyC}/f_{net}. \qquad (8)$$

5.3. Our Updated List of GH II Regions

We created probability distribution functions (PDFs) based upon the values and errors for all input variables given in Table 5, as well as for the constants R_0 and a_o, and the intermediary variable $x\sigma_{He}/x_1\sigma_\nu$. For input values with the same upper and lower uncertainties (i.e., reported with a standard deviation), the PDFs were created using a normal distribution (with width determined by the standard deviation). For values with asymmetric uncertainties, we created a PDF from two half Gaussians whose width is determined by the two uncertainties and normalized to the same peak. We created a Monte Carlo code that chose values randomly from each of these PDFs and used them as the inputs for the equations in Section 5.2 and repeated this 25,000 times. From the posterior PDFs generated by this process, the most likely (mode) values given in Table 7 are listed for the observed Lyman continuum photon rate (N'_{LyC}), electron density (N_e), galactocentric distance (R_{GC}), and intrinsic Lyman continuum photon rate (N_{LyC}) for all sources. These posterior PDFs for the above parameters were almost always skewed somewhat, so in order to calculate the uncertainties in the mode values, we determined the lower and upper bounds of the PDF such that the value of the PDF was equal at both bounds and the area under the PDF between the two bounds was equal to 68.2% of the area under the total PDF. This is analogous to the standard deviation of a normal distribution which also represents a 68.2% confidence interval. To help visualize this, we provide in Figure 8 graphs of one of the input distributions with asymmetric errors (distance to the Sun), as well as two example output distributions (R_{GC} and N_{LyC}) with the mode, mean, and calculated 68.2% confidence intervals shown. These uncertainties are reported for all values given in Table 7.

We preserve the input values from Conti & Crowther (2004) for 6 cm flux density ($S_{6\,cm}$; Table 5, Column 8) and 6 cm source size ($\theta_{6\,cm}$; Table 5, Column 9) since the surveys that performed these observations are from the single-dish radio antennas with the ability to resolve sources equal to or greater than $\sim 2'$, which is adequate for the typical sizes of GH II regions. More recent radio continuum observations have been taken of several of these GH II regions, many with subarcsecond resolutions; however, these observations are taken with interferometric arrays and thus are not as good for observing extended large-scale emission, which is filtered out to varying degrees.

Generally, even distances that are determined with extreme accuracy via say, maser parallaxes, are within reasonable agreement with either the near or far kinematic distance. As Sgr D and W42 show us, the largest changes in the calculation of N_{LyC} is when a source distance is changed from a far distance to near. Therefore the most impactful measurements since Conti & Crowther (2004), and those that will change the GH II region census the most, will be those that help to resolve near/far kinematic distance ambiguities by changing the accepted distance from far to near. That being said, however, there are a good number of sources in our updated list that fall relatively close to the $N_{LyC} = 10^{50}$ photons s^{-1} criterion, so a proper estimate of the errors for each source was warranted in order to clearly indicate how likely a source is or is not a GH II.

One additional caveat is that we assumed in Section 5.2 an R_0 of 8.34 ± 0.16 kpc; however, the IAU recommended value is 8.5 kpc, and there exist recent measurements that place the Galactic Center as close as 7.9 kpc (VERA Collaboration et al. 2020). Using an inaccurate R_0 value does not affect the calculations of N'_{LyC} or N_e, and only affects the calculations of R_{GC} and N_{LyC}. The difference in these values when one assumes $R_0 = 8.5$ kpc versus 7.9 kpc, is up to ± 0.6 kpc in the calculation of R_{GC} and ± 0.03 dex in the calculation of $\log N_{LyC}$.

Table 7
Derived GH II and H II Region Properties

| Name	N'_{LyC} $\log(\mathrm{s}^{-1})$	N_e (cm^{-3})	R_{GC} (kpc)	N_{LyC} $\log(\mathrm{s}^{-1})$	Is GH II?
G0.361-0.780	$49.76^{+0.10}_{-0.11}$	38^{+5}_{-6}	$0.06^{+0.23}_{-0.01}$	$50.06^{+0.17}_{-0.15}$	Likely
G0.394-0.540	$49.76^{+0.09}_{-0.07}$	38^{+6}_{-4}	$0.06^{+0.21}_{-0.01}$	$50.07^{+0.15}_{-0.12}$	Likely
G0.489-0.668	$49.78^{+0.12}_{-0.09}$	65^{+13}_{-8}	$0.08^{+0.32}_{-0.01}$	$50.15^{+0.17}_{-0.16}$	Likely
Sgr B1	$50.31^{+0.14}_{-0.07}$	146^{+22}_{-20}	$0.10^{+0.83}_{-0.01}$	$50.87^{+0.22}_{-0.22}$	Yes
G0.572-0.628	$49.70^{+0.10}_{-0.09}$	117^{+15}_{-19}	$0.09^{+0.24}_{-0.00}$	$50.08^{+0.18}_{-0.15}$	Likely
Sgr D	$49.15^{+0.19}_{-0.16}$	99^{+18}_{-13}	$5.95^{+0.45}_{-0.58}$	$49.37^{+0.19}_{-0.27}$	No
G2.303+0.243	$50.22^{+0.15}_{-0.13}$	22^{+4}_{-3}	$5.07^{+1.06}_{-0.67}$	$50.48^{+0.20}_{-0.19}$	Yes
G3.270-0.101	$50.30^{+0.07}_{-0.06}$	30^{+4}_{-3}	$6.07^{+0.73}_{-0.88}$	$50.55^{+0.16}_{-0.13}$	Yes
G4.412+0.118	$50.40^{+0.12}_{-0.09}$	36^{+5}_{-5}	$6.78^{+0.70}_{-0.67}$	$50.69^{+0.19}_{-0.18}$	Yes
M8	$49.29^{+0.07}_{-0.06}$	227^{+31}_{-28}	$7.00^{+0.18}_{-0.17}$	$49.52^{+0.14}_{-0.15}$	No
G8.137+0.228	$48.99^{+0.07}_{-0.12}$	318^{+42}_{-27}	$5.04^{+0.37}_{-0.33}$	$49.20^{+0.15}_{-0.17}$	No
W31-South	$49.90^{+0.08}_{-0.09}$	446^{+53}_{-56}	$5.01^{+0.35}_{-0.31}$	$50.32^{+0.20}_{-0.22}$	Yes
W31-North	$48.82^{+0.13}_{-0.14}$	303^{+48}_{-33}	$6.58^{+0.35}_{-0.24}$	$48.97^{+0.22}_{-0.16}$	No
M17	$50.49^{+0.07}_{-0.07}$	1114^{+144}_{-119}	$6.43^{+0.21}_{-0.19}$	$51.02^{+0.36}_{-0.25}$	Yes
G20.733-0.087	$50.48^{+0.05}_{-0.06}$	40^{+6}_{-4}	$4.85^{+0.30}_{-0.33}$	$50.80^{+0.16}_{-0.15}$	Yes
W42	$49.24^{+0.25}_{-0.29}$	237^{+63}_{-38}	$6.56^{+0.37}_{-0.83}$	$49.44^{+0.33}_{-0.35}$	No
G29.944-0.042	$49.95^{+0.09}_{-0.08}$	142^{+21}_{-18}	$4.37^{+0.21}_{-0.17}$	$50.31^{+0.16}_{-0.19}$	Yes
W43	$50.30^{+0.08}_{-0.07}$	199^{+24}_{-25}	$4.53^{+0.21}_{-0.15}$	$50.76^{+0.18}_{-0.22}$	Yes
G32.80+0.19	$49.96^{+0.05}_{-0.05}$	96^{+16}_{-11}	$7.41^{+0.31}_{-0.31}$	$50.23^{+0.13}_{-0.17}$	Yes
W49A	$50.92^{+0.08}_{-0.07}$	240^{+31}_{-26}	$7.57^{+0.53}_{-0.44}$	$51.42^{+0.25}_{-0.28}$	Yes
G48.596+0.042	$50.15^{+0.09}_{-0.10}$	62^{+9}_{-8}	$8.18^{+0.38}_{-0.37}$	$50.38^{+0.18}_{-0.18}$	Yes
G48.9-0.3	$49.85^{+0.11}_{-0.08}$	114^{+15}_{-14}	$6.31^{+0.12}_{-0.13}$	$50.16^{+0.15}_{-0.20}$	Likely
W51A:G49.4-0.3	$49.87^{+0.08}_{-0.06}$	249^{+27}_{-33}	$6.32^{+0.14}_{-0.11}$	$50.22^{+0.15}_{-0.20}$	Yes
W51A:G49.5-0.4	$50.51^{+0.08}_{-0.07}$	468^{+72}_{-48}	$6.34^{+0.13}_{-0.11}$	$51.03^{+0.24}_{-0.27}$	Yes
K3-50(W58A)	$49.84^{+0.08}_{-0.11}$	220^{+41}_{-32}	$9.22^{+0.44}_{-0.31}$	$50.07^{+0.19}_{-0.17}$	Likely
DR7	$49.90^{+0.12}_{-0.10}$	117^{+20}_{-16}	$10.10^{+0.40}_{-0.52}$	$50.10^{+0.14}_{-0.18}$	Likely
W3	$49.57^{+0.09}_{-0.08}$	461^{+76}_{-62}	$10.09^{+0.21}_{-0.22}$	$49.78^{+0.14}_{-0.17}$	No
RCW 42	$50.17^{+0.12}_{-0.13}$	261^{+35}_{-33}	$9.95^{+0.47}_{-0.45}$	$50.42^{+0.19}_{-0.18}$	Yes
RCW 46	$50.17^{+0.12}_{-0.12}$	170^{+30}_{-21}	$9.09^{+0.36}_{-0.36}$	$50.44^{+0.22}_{-0.20}$	Yes
RCW 49	$50.64^{+0.07}_{-0.07}$	194^{+33}_{-21}	$8.39^{+0.12}_{-0.19}$	$51.08^{+0.18}_{-0.26}$	Yes
NGC 3372	$49.90^{+0.06}_{-0.06}$	216^{+24}_{-28}	$7.97^{+0.15}_{-0.16}$	$50.20^{+0.15}_{-0.19}$	Yes
G289.066-0.357	$49.87^{+0.11}_{-0.10}$	53^{+8}_{-7}	$8.93^{+0.36}_{-0.36}$	$50.07^{+0.14}_{-0.20}$	Likely
NGC 3576	$49.95^{+0.10}_{-0.11}$	786^{+140}_{-88}	$7.77^{+0.16}_{-0.14}$	$50.30^{+0.26}_{-0.21}$	Yes
NGC 3603	$51.15^{+0.05}_{-0.05}$	159^{+25}_{-14}	$8.77^{+0.13}_{-0.09}$	$51.61^{+0.26}_{-0.25}$	Yes
G298.227-0.340	$50.84^{+0.13}_{-0.12}$	130^{+25}_{-14}	$11.19^{+1.30}_{-1.25}$	$51.11^{+0.20}_{-0.19}$	Yes
G298.862-0.438	$50.85^{+0.12}_{-0.14}$	119^{+22}_{-13}	$11.15^{+1.18}_{-1.37}$	$51.09^{+0.21}_{-0.17}$	Yes
G305.359+0.194	$49.97^{+0.19}_{-0.22}$	279^{+58}_{-47}	$6.88^{+0.24}_{-0.16}$	$50.32^{+0.24}_{-0.35}$	Likely
G319.158-0.398	$50.17^{+0.06}_{-0.05}$	34^{+4}_{-4}	$7.39^{+0.22}_{-0.29}$	$50.43^{+0.12}_{-0.17}$	Yes
G319.392-0.009	$50.10^{+0.05}_{-0.07}$	66^{+9}_{-9}	$7.74^{+0.20}_{-0.34}$	$50.32^{+0.17}_{-0.14}$	Yes
G320.327-0.184	$47.67^{+0.33}_{-0.48}$	116^{+43}_{-24}	$7.84^{+0.27}_{-0.30}$	$47.73^{+0.30}_{-0.58}$	No
RCW 97	$49.85^{+0.07}_{-0.13}$	441^{+66}_{-48}	$6.10^{+0.26}_{-0.25}$	$50.16^{+0.24}_{-0.18}$	Likely
G327.993-0.100	$48.70^{+0.12}_{-0.10}$	160^{+20}_{-23}	$6.14^{+0.27}_{-0.26}$	$48.84^{+0.17}_{-0.15}$	No
G330.868-0.365	$49.35^{+0.11}_{-0.12}$	117^{+18}_{-14}	$5.53^{+0.33}_{-0.31}$	$49.58^{+0.15}_{-0.20}$	No
G331.324-0.348	$48.99^{+0.16}_{-0.16}$	256^{+38}_{-31}	$5.64^{+0.47}_{-0.41}$	$49.19^{+0.23}_{-0.21}$	No
G331.354+1.072	$49.20^{+0.11}_{-0.08}$	51^{+8}_{-6}	$4.87^{+0.23}_{-0.34}$	$49.38^{+0.16}_{-0.14}$	No
G331.529-0.084	$50.48^{+0.24}_{-0.29}$	153^{+31}_{-30}	$4.03^{+0.54}_{-0.15}$	$50.97^{+0.30}_{-0.44}$	Yes
G333.122-0.446	$49.56^{+0.09}_{-0.07}$	214^{+32}_{-20}	$6.13^{+0.23}_{-0.22}$	$49.84^{+0.18}_{-0.16}$	Unlikely
G333.293-0.382	$49.56^{+0.22}_{-0.25}$	266^{+58}_{-46}	$6.11^{+0.57}_{-0.57}$	$49.87^{+0.27}_{-0.37}$	Unlikely
G333.610-0.217	$49.99^{+0.19}_{-0.30}$	451^{+97}_{-82}	$6.18^{+0.55}_{-0.60}$	$50.30^{+0.35}_{-0.35}$	Likely
G338.398+0.164	$50.68^{+0.04}_{-0.06}$	52^{+6}_{-6}	$6.30^{+0.27}_{-0.38}$	$51.04^{+0.16}_{-0.18}$	Yes
G338.400-0.201	$50.17^{+0.05}_{-0.06}$	54^{+8}_{-7}	$8.47^{+0.61}_{-0.34}$	$50.38^{+0.16}_{-0.16}$	Yes
G345.555-0.043	$50.58^{+0.06}_{-0.05}$	38^{+4}_{-4}	$7.49^{+0.58}_{-0.35}$	$50.89^{+0.14}_{-0.18}$	Yes
G345.645+0.009	$50.39^{+0.05}_{-0.05}$	50^{+6}_{-5}	$7.10^{+0.47}_{-0.38}$	$50.68^{+0.15}_{-0.16}$	Yes
G347.611+0.204	$50.28^{+0.10}_{-0.11}$	50^{+8}_{-6}	$1.80^{+0.20}_{-0.06}$	$50.67^{+0.16}_{-0.19}$	Yes
G351.467-0.462	$48.69^{+0.11}_{-0.08}$	132^{+21}_{-14}	$5.19^{+0.28}_{-0.39}$	$48.88^{+0.13}_{-0.16}$	No
Sgr C	$50.09^{+0.05}_{-0.05}$	87^{+12}_{-8}	$0.09^{+0.18}_{-0.00}$	$50.51^{+0.14}_{-0.14}$	Yes
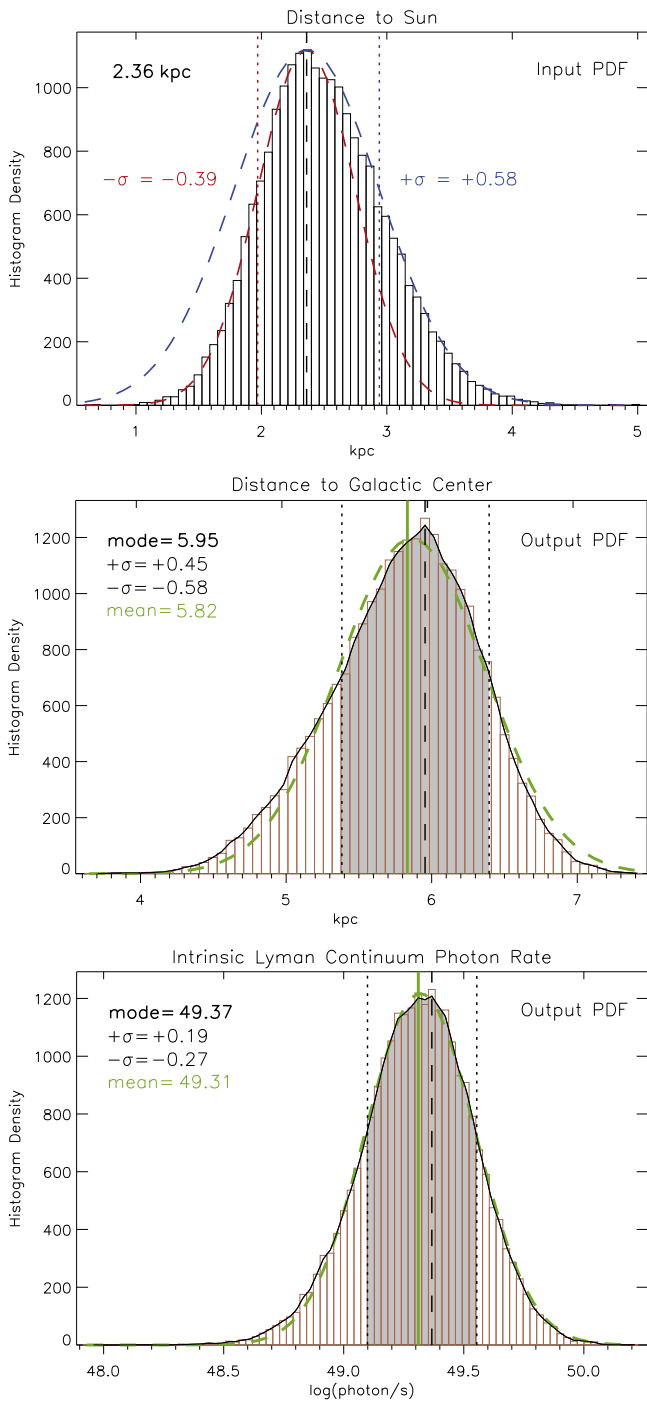
Figure 8. Input and output PDFs for select values associated with the Monte Carlo calculations for Sgr D. The top plot demonstrates graphically how the input PDFs were created for values with asymmetric uncertainties, in this case for the the source distance. The dashed red curve shows the Gaussian fit to the lower uncertainty and the blue dashed curve for the upper uncertainty. The black dashed vertical line is the value for the distance to Sgr D, and the red and blue dotted vertical lines show the lower and upper uncertainty bounds, respectively. The bottom two plots show two example output (posterior) PDFs, for the distance to the Galactic center (R_{GC}) and intrinsic Lyman continuum photon rate (N_{LyC}). The black line is the fit to the histogram of the PDF, the black dashed vertical line shows the mode of the PDF. The shaded area shows the 68.2% confidence interval, and the upper and lower bounds of this area are given by the dotted vertical lines (which represent the upper and lower uncertainties, respectively). The mode values and these upper and lower uncertainties for all sources and all output parameter PDFs are given in Table 7. For comparison, the green dashed lines are simple Gaussian fits to the black curves, and the vertical green lines show the mean values calculated from those fits.

Conti & Crowther ([2004](#)) define a GH II as a source with $N_{LyC} > 10^{50}$ photons s^{-1} and we find that with our new calculations that many sources no longer satisfy that criterion (see the rightmost Column of Table 7). Of the 56 sources in the original census, we find that 12 can no longer be considered GH II regions. An additional two sources have N_{LyC} values below the 10^{50} photons s^{-1} criterion, but their upper limit errors do cross over this cutoff value. These sources are considered "Unlikely" to be GH II regions in Table 7. There are a further 11 regions where their N_{LyC} values are above the cutoff criterion, but the lower limits errors do go below the cutoff value. These sources are considered "Likely" to be GH II regions in Table 7.

Related to this cutoff value, however, is the question of whether or not the GH II criterion of $\log N_{LyC} > 50.0$ photons s^{-1} should be a strict or loose criterion. Conti & Crowther ([2004](#)) claim that this number was chosen because it was close to the equivalent of 10 O7V stars. Whether or not this is true depends on the stellar models used (e.g., this is about 14 O7V stars according to Panagia [1973](#)). Giant H II regions were first defined, in an admittedly arbitrary fashion, by Mezger ([1970](#)) as having $S_5 d^2 > 400$, with S_5 being the 5 GHz (i.e., 6 cm) radio flux density in Jansky, and d the distance to the source in kiloparsecs. Plugging 400 in for the last two terms in Equation ([1](#)) and assuming $T_e = 10,000$ K yields the criterion used by Smith et al. ([1978](#)) of GH II regions requiring $\log N'_{LyC} > 49.6$ (i.e., defined by the observed rather than intrinsic Lyman continuum photon rate). Looking to the $\log N'_{LyC}$ values we derived for the sources in Table 7, it can be seen that all sources with $\log N'_{LyC} > 49.6$ also have $\log N_{LyC} > 50.0$, and thus it would seem that setting the criteria based upon an intrinsic or observed Lyman continuum photon rate does not greatly change which sources are considered to be, or not to be, GH II regions.

There are also an additional three sources with significant unresolved ambiguity. As pointed out in Table 6 and the [Appendix](#), G320.327-0.184 and G338.398+0.164 have kinematic distances with conflicting absorption line measurements pointing to both near and far distances. G320.327-0.184 was chosen to be at the near distance because the H I observations are more recent. G338.398+0.164 has multiple ATLASGAL submillimeter clumps within the radio emission region with different indicated near/far distances from H I absorption measurements, but the central source has H I absorption indicating the far distance. G338.400-0.201 is uncertain because there is a wide range of measured v_{lsr} values, some of which indicate the region is in the far outer Galaxy; however, the infrared component as seen by MSX is compact and relatively faint, which is highly unusual for a GH II region. Nonetheless, we keep the far distance in keeping with previous studies.

To summarize, 42 of the original census of 56 GH II regions appear to be, or are likely to be, GH II regions. This means that 25% of the original census is below the cutoff $\log N_{LyC}$ value to be considered bona fide GH II regions. Furthermore, another 20% of the original census have errors that dip below the cutoff value, so their status as a bona fide GH II is less certain. We stress that while the original census of GH II regions compiled by Conti & Crowther ([2004](#)) was the most extensively vetted list available, it is not considered a complete list of all radio GH II regions in the Milky Way. While it would be interesting to do a more thorough compilation of all GH II sources

(including revisiting the sources originally rejected by Conti & Crowther 2004), this census (even our new pared-down version) does contain the brightest and most well-known sources, and contains a sufficient number of sources for the purposes of our SOFIA survey.

6. Discussion

As discussed in Conti & Crowther (2004) and the introduction to this paper, apart from having Lyman continuum photon rates in excess of $N_{\rm LyC} = 10^{50}$ photons s^{-1}, GH II regions are also considered to be the formation sites of our Galaxy's most massive OB clusters. Certainly, the highest values of $N_{\rm LyC}$ observed in some GH II regions (e.g., NGC 3603) cannot physically be due to a single O-type star, and must be due to a sizable cluster or multiple generations of clusters of massive, ionizing stars. However, as one goes to lower values of $N_{\rm LyC}$ it can become unclear if the region is predominantly powered by a single, very massive star or a cluster of less-massive ionizing stars. Generally speaking, as we go to earlier and earlier O-star spectral types, they rapidly become increasingly rare, and therefore the derived $N_{\rm LyC}$ value for modestly powerful H II regions becomes less likely to be due to a single, powerful O-star and more likely to be due to a cluster of stars with the combined ionizing rate equal to that same $N_{\rm LyC}$ value. However, this is not always going to be the case, as we see in the examples of W42 and Sgr D in this work where they appear to be predominantly ionized by a single source. Therefore, because all H II regions lie on a continuum of $N_{\rm LyC}$ values, any cutoff value is arbitrary and alone may not be sufficient to ascertain whether a region's energy is dominated by a very powerful ionizing source, or a large cluster of less-powerful (but still massive) ionizing sources (i.e., a large OB cluster or protocluster).

Another example of this comes from looking at the sources rejected as GH II regions in Table 7, where we see that one of the sources with the smallest measured $\log N_{\rm LyC}$ is G351.467-0.462, with a value of 48.88 photons s^{-1}. This is the equivalent of a single main-sequence O7 star of $\sim 30\,M_{\odot}$. This, of course, does not by itself mean that there is definitively only one O7 star ionizing G351.467-0.462. In principle, however, G351.467-0.462 could indeed be a H II region powered by a single O7 ionizing star, rather than a star-forming region producing an OB stellar cluster (with, e.g., ~ 30 B0 stars, which is also equivalent to $\log N_{\rm LyC} = 48.88$ photons s^{-1}). A well-known analog would be θ^1 Orionis C1, which is an O6V star (Balega et al. 2014) that is singularly responsible for generating the vast majority of the ionizing photons in the Orion Nebula ($\log N_{\rm LyC} = 49.47$ photon s^{-1}; Inoue et al. 2001). Though the Orion Nebula is impressive due to its proximity, there is a stark contrast between Orion and the most powerful object in the Milky Way, NGC 3603. By way of comparison, NGC 3603 has the equivalent of ~ 100 times the $N_{\rm LyC}$ of Orion, and 10 times the number of revealed O stars (i.e., 50 stars $\geqslant 15\,M_{\odot}$ compared to five; Hillenbrand 1997; Eisenhauer et al. 1998). Also by way of comparison, the $N_{\rm LyC} = 10^{50}$ photons s^{-1} cutoff is the equivalent to 4 times that of Orion or the equivalent of single O4 ZAMS star (Panagia 1973) with a mass of $65\,M_{\odot}$ (Blum et al. 2000).

We can look at the multiwavelength observations of Sgr D and W42 and see if there is any supporting evidence (beyond just $N_{\rm LyC}$) that would demonstrate that these two regions, in particular, are not likely to be GH II regions. Indeed,

qualitatively Sgr D and W42 have much simpler morphologies compared to our previously observed GH II regions of this project: G49.5-0.4 and G49.4-0.3 in W51A (Paper I), M17 (Lim et al. 2020), and W49A (De Buizer et al. 2021). The radio and mid-infrared emission from both Sgr D and W42 are dominated by a single, bright, and relatively compact region. Besides the extended source associated with the main infrared peak, Sgr D has only two other extended (but diffuse) infrared sources (source A and source 2), while W42 has no other separate, extended infrared sources in its vicinity. This can be contrasted with the previously studied GH II regions, which are broken up into multiple, bright, extended, and separate star-forming subregions such as G49.5-0.4 and G49.4-0.3 in W51A (10 and five subregions, respectively), W49A (15 subregions), or M17 (four subregions). Besides the extended mid-infrared emission sources associated with Sgr D and W42, there are three compact mid-infrared sources in Sgr D (sources B–D) and two in W42 (W42-MME and source 1). This is far fewer than the number of compact sources seen in our previously studied GH II regions G49.5-0.4 (37), G49.4-0.3 (10), W49A (24), and M17 (16), which lie at a wide range of distances (i.e., $\sim 2-11$ kpc). The dearth of compact sources within Sgr D and W42 would seem to imply less-vigorous star formation activity (regardless of their distances) than what we see in the GH II regions studied thus far. Furthermore, the best-fit mass estimates of the most massive YSOs in Sgr D and W42 (Table 4) are only 16 and $32\,M_{\odot}$, respectively, which is more modest compared to the largest best-fit masses of the MYSOs seen in M17 ($64\,M_{\odot}$), W49A ($128\,M_{\odot}$), G49.5-0.4 ($96\,M_{\odot}$), and G49.4-0.3 ($64\,M_{\odot}$).

If Sgr D and W42 have such low $N_{\rm LyC}$, we might suspect that they are likely to be like Orion and have a single O-star responsible for the majority (if not all) of their emission. In fact, in the case of W42 there is a confirmed O-star seen in the near-infrared that has the equivalent $N_{\rm LyC}$ of the entire H II region and is therefore overwhelmingly responsible for ionizing the entire region (Blum et al. 2000). A H II region predominantly ionized by a single star would also mean that the majority of the associated mid-infrared dust emission should be concentrated around a single peak, as is the case for Sgr D and W42, rather than coming from multiple, separate, star-forming clumps. Quantitatively, the percentage of the flux in the brightest peak compared to the total flux in the whole H II region is $\sim 85\%$ for Sgr D and $\sim 50\%$ for W42 at 37 μm. This can be compared to the GH II regions we have already studied that have more dispersed flux spread throughout their entire volume and/or are broken up into multiple star-forming subregions. The percentage of the flux in the brightest peak to the total flux in the whole GH II region is $\sim 20\%$ for G49.5-0.04, $\sim 15\%$ for G49.4-0.03, $\sim 25\%$ for W49A, and $\sim 5\%$ for M17 at 37 μm.

In summary, the case studies of Sgr D and W42 reveal that they have multiwavelength properties that are in keeping with the idea that they are more modest H II regions accompanied by less-vigorous star formation activity, rather than being like our previously studied GH II regions (i.e., G49.5-0.4 and G49.4-0.3 in W51A, M17, and W49A). In particular, since the majority of the infrared (and/or radio) flux in the entire H II region comes from a single, compact region in both these objects, it indicates that they are predominantly powered by a single ionizing source (similar to Orion) rather than a massive OB cluster or protocluster. For some sources with large errors in their derived $N_{\rm LyC}$ values or large uncertainties in their distances, one could

potentially use similar analyses to be able to differentiate between sources likely to be (or not to be) GH II regions. However, we caution that this proposed distinction between GH II and H II regions is only based upon a small number of sources (i.e., four GH II regions and two H II regions), and the GH II and H II regions likely have some variety of properties that cannot be accounted for with such small numbers. As we continue our survey of GH II regions, we will address the observational properties as a function of N_{LyC} in a later paper when there are more sources to be of statistical significance to make more nuanced conclusions about the GH II and H II populations as a whole.

7. Summary

In the first part of this paper we present the new SOFIA infrared imaging data that we obtained for Sgr D at 20 and 37 μm and W42 at 25 and 37 μm. We discuss how the updated, nearer distances measured toward both Sgr D and W42 disqualify them as being bona fide GH II regions. Nonetheless, we derive and discuss the detailed physical properties of the individual compact sources and subregions as well as the large-scale properties of the two star-forming regions based upon the SOFIA data and other multiwavelength data.

While the radio region of Sgr D is a fairly circular $6\rlap{.}'6$ diameter H II region, bright mid and far-infrared emission only comes from a small number of discrete locations. For Sgr D, we suggest that the three brightest mid-infrared sources, sources 2, 3, and D, are all coincident with (and likely formed out of) a dark filament induced by the collision of the Sgr D H II region with SNR G1.05-0.15. Within Sgr D we find only three MYSO candidates. The brightest mid-infrared source, source 3, appears to be at least partially embedded in the dark filament and has an infrared morphology similar to an edge-on flared disk.

Our SOFIA images of W42 at 25 and 37 μm detect a single, extended emission region with an extent similar to that seen by MSX at 22 μm, i.e., about 2′ in diameter. The central 30″ region of W42 has a bright mid-infrared peak coincident with a known radio compact H II region (G025.3824-00.1812), a second peak coincident with methanol maser emission (a tracer of high-mass YSOs), and a third peak to the north associated with fainter radio continuum emission. However, there is an O5-O6.5 star (W42#1) near the center of W42 (Blum et al. 2000), whose Lyman continuum photon rate alone is equal to that of the entirety of W42. Due to its more evolved nature, it apparently does not have much circumstellar dust since it has no detectable mid-infrared emission of its own as seen by SOFIA. It is unclear how much of the radio and infrared emission attributed to the sources associated with the infrared and radio peaks may actually be due to external ionization and heating by W42#1, but it does appear that W42#1 may be solely responsible for the ionization of the vast majority of W42. Our SED modeling shows three massive YSOs may be present here; however, this assumes no contamination from W42#1, which may not be the case.

In the second part of this paper we compiled data that updated the distances to the census of 56 GH II regions identified by Conti & Crowther (2004). We recalculated their Lyman continuum photon rates, N_{LyC}, and determined that 25% of these sources (14) are at sufficiently closer distances that their derived values of using the measurement with the lowest error N_{LyC} are $<10^{50}$ photons s^{-1}, meaning they no longer meet the criterion to be considered GH II regions in the strictest sense. Of the remaining 42 GH II region candidates identified here, an additional 20% (11) have $N_{LyC} > 10^{50}$ photons s^{-1} but have measurement errors that could place them below the cutoff value for being bona fide GH II regions.

We additionally looked at other observational and physical characteristics (besides Lyman continuum photon rate) of Sgr D and W42 and compared these properties to those of the GH II regions that we have already studied as part of the SOFIA GH II region survey. We determine that Sgr D and W42 appear to have much simpler morphologies in the infrared, seem to have a dearth of compact infrared sources, and have observational characteristics that indicate that they are dominantly ionized by single massive stars and not large OB clusters. Additionally, the most massive MYSOs in Sgr D and W42 are only 16 and 32 $M_{\odot}$, respectively, while our previous observations of the brightest GH II regions have the most massive MYSOs in the range of 64–128 $M_{\odot}$. Given that the Lyman continuum photon rate for a single H II region exists within a continuum of N_{LyC} values provided by the population of all H II regions, any cutoff value is somewhat arbitrary. We suggest, based upon what we have learned from Sgr D and W42, that if a source has a derived value near the N_{LyC} cutoff and/or has large uncertainty in this value or its distance, other observational indicators such as those described above could potentially be used to help determine if it should be disqualified as a bona fide GH II region.

Appendix
Discussion of Distance Determinations for Each Region

G0.361-0.780/G0.394-0.540/G0.489-0.668/G0.572-0.628: These four sources all lie within a 10′ area centered at $(\ell, b) = (0.45, -0.67)$, in a dusty complex that lies at a similar Galactic longitude as Sgr B but more than a half a degree below the plane of the central Galaxy described by Sgr B, Sgr A, and Sgr C. For these sources there exist kinematic distance determinations only, and in and around the Galactic center $(357.5 < \ell < 2.5)$ such measurements are not reliable because the sources have more complex orbits than those for sources that lie in the Galactic disk at larger galactocentric radii (Wenger et al. 2018). Thus, in many studies such Galactic Center sources are simply assumed to be the same distance as Sgr A*. However, as we see in the case of Sgr D this is not always an accurate assumption. Observations of H110α by Downes et al. (1980) toward each of these sources yield v_{lsr} values between 17 and 24 km s^{-1}, for which we calculate near kinematic distances between 7.66 and 8.0 kpc; far distances are

nearly the same and range from 8.30–8.48 kpc. The only one of these sources with observed absorption features is G0.572-0.628; however, Jones et al. (2013) state that the observed H I absorption seen toward this source does not give conclusive evidence for resolving the distance ambiguity. Hou & Han (2014) adopt the near distances to all of these sources and reference Russeil (2003) as the source of the disambiguation. Russeil (2003) state that the near distances are preferred as these sources exhibit an Hα counterpart. We will assume these near distances here as well.

Sgr B1: The source closest to the radio region galactic coordinates ($\ell = 0.518$, $b = -0.065$) given by Conti & Crowther (2004) is Sgr B1 (which is coincident to within an arcminute). However, these coordinates were identified as W24 by Conti & Crowther (2004), which is usually synonymous with Sgr B2, though that source is $9'$ away from Sgr B1. Though these separations seem quite large, both Sgr B1 and Sgr B2 are believed to be part of the same molecular cloud (Simpson et al. 2021) and have similar v_{lsr} velocities. The distance to Sgr B2 was determined via maser parallax to be $7.8^{+0.8}_{-0.7}$ kpc, and it is assumed here that this distance applies to Sgr B1 as well.

G2.303+0.243: Because OH absorption lines are found with velocities ($\sim 16 \, km \, s^{-1}$) greater than those of the source ($5 \, km \, s^{-1}$), Russeil (2003) adopt the far distance to this source. Using the most precise velocity measurement, $v_{lsr} = 4.9 \pm 0.7 \, km \, s^{-1}$, which is the H87α+H88α transition from Lockman (1989), we derive a kinematic far distance of 13.48 kpc.

G3.270-0.101: The H110α measurement of Downes et al. (1980) toward this source has a v_{lsr} value of 4.3 ± 5.0 kpc; however, we will use the comparable but more precise measurement in the H87α+H88α transitions from Lockman (1989) of $v_{lsr} = 4.9 \pm 0.8 \, km \, s^{-1}$. This velocity yields a far kinematic distance of 14.33 kpc, which we adopt here given that Jones et al. (2013) state that there are H I absorption features seen at velocities corresponding to both the Near and Far 3 kpc Arms, suggesting a distance at least as far as the Far 3 kpc Arm.

G4.412+0.118: This is a source that has a 6 cm radio diameter of almost $5'$, but there are multiple molecular clumps within even $2'$ of the Galactic coordinates of this source. The closest source in the ATLASGAL catalog (Rathborne et al. 2016) is $0'.6$ away and has a N_2H^+ velocity of $4.23 \pm 0.25 \, km \, s^{-1}$; however, there are two other sources within $2'$ of this location with values of 3.0 and $8.5 \, km \, s^{-1}$. The H110α measurement of Downes et al. (1980) toward this source has a v_{lsr} value of $5.7 \pm 5.0 \, km \, s^{-1}$, and the more precise observations of the H87α+H88α transitions from Lockman (1989) give $v_{lsr} = 4.1 \pm 0.9 \, km \, s^{-1}$. Jones et al. (2013) claim this source is likely at the far kinematic distance due to H I absorption present at multiple velocities, and quote distance (with large errors) of 15.6 ± 8.9 kpc. Using our adopted value of $4.23 \, km \, s^{-1}$ (chosen for it is precision) we calculate a far distance of $14.97^{+0.77}_{-0.58}$ kpc. The far distance is also suggested by Russeil (2003) due to absorption features seen at velocities greater than that of the source.

M8: The v_{lsr} of this source has been observed by multiple groups in multiple transitions in the past 50 years. Choosing from one of the papers we have cited previously in this work, Lockman (1989) measured a $v_{lsr} = 4.1 \pm 0.9 \, km \, s^{-1}$ in the H87α +H88α transition, and the source was believed to be at the near kinematic distance due to its low Galactic latitude (i.e., $-1.178°$).

Moisés et al. (2011) claim that their spectrophotometry of sources within M8 agree with the near kinematic distance of 2.8 kpc claimed by Russeil (2003). However, SED fitting to near-infrared sources in M8 performed by Arias et al. (2006) have estimated an even closer distance of 1.25 kpc. Indeed the most recent measurements made using GAIA parallaxes of cluster members within M8 support this closer distance, for instance, Binder & Povich (2018) measuring 1.17 ± 0.10 kpc, Damiani et al. (2019) measuring 1.325 ± 0.113 kpc, as well as our adopted value of 1.34 ± 0.07 kpc measured by Ramírez-Tannus et al. (2020).

G8.137+0.228: There have been many observations of the v_{lsr} of this source in multiple hydrogen transitions as well as molecule CS, leading to values between 19.3 and $24.4 \, km \, s^{-1}$ (see Hou & Han 2014). We adopt the velocity measurement with the smallest error of $v_{lsr} = 20.31 \pm 0.06$ from Quireza et al. (2006). Conti & Crowther (2004) adopted the far distance to this source; however, most recent studies prefer the closer distance (e.g., Urquhart et al. 2018; Dewangan et al. 2019). Jones et al. (2013) claim that a nearside kinematic value is preferred because they do not see any H I absorption features.

W31: W31 consists of multiple extended H II regions, of which G10.315-0.150 (W31-North), G10.159-0.349 (W31-South), and G10.62-0.38 are the brightest in centimeter radio continuum emission. A distance determination to W31 is very complicated. For W31-South, Conti & Crowther (2004) provide a distance of 4.5 kpc, which is from Corbel & Eikenberry (2004). That work claims that because several measurements have shown absorption lines observed up to $43 \, km \, s^{-1}$ (e.g., Wilson 1974), a distance less than ~ 2.5 kpc derived by some kinematic studies would not make sense, and that at $43 \, km \, s^{-1}$ the source would exist at 4.5 kpc. However, from Urquhart et al. (2018) it can be seen that there are five ATLASGAL clumps within $2'$ of these Galactic coordinates (and the source has a measured 6 cm radio diameter of $2'.9$). The closest clump ($\sim 0'.6$ away) has a v_{lsr} of $8.9 \, km \, s^{-1}$, while all the others have v_{lsr} of $13.0–14.4 \, km \, s^{-1}$. Therefore, there are likely to be multiple clumps present at different distances along the line of sight to this source that are confusing the issue. Contrary to Corbel & Eikenberry (2004), Urquhart et al. (2018) claim that the H I self-absorption observations argue for a near kinematic value for the closest ATLASGAL clump and provide a kinematic distance of 1.3 kpc.

Luckily, the distance to this source has been measured by what is generally considered a more accurate method. That is, there have been two spectrophotometric distance measurements toward the NIR-bright stars within W31-South, the first by Blum et al. (2001), who derive a spectrophotometric distance of 3.4 ± 0.3 kpc, and the second by Moisés et al. (2011), who derive a distance of 3.55 ± 0.94 kpc. We will adopt here the more accurate spectrophotometric distance of Blum et al. (2001). As we discuss in Section 5.1, the fact that this value does not match either the kinematic distance, nor the H I absorption velocities, is not uncommon.

Similarly for W31-North, Deharveng et al. (2015) discuss in-depth the multitude of conflicting distance measurements that lead to a distance range of 2–19 kpc, but argue based upon their spectrophotometric analysis that the region lies at a distance of 1.75 ± 0.25 kpc, which is compatible with the near kinematic distance. For W31-North, we again adopt the spectrophotometric distance due to the fact that the methodology is more accurate than the kinematically derived distances.

Though it is not in our source list, the third major region within W31, G10.62-0.38, has had accurate maser parallax measurements performed by Sanna et al. (2014), placing it at $4.95^{+0.51}_{-0.43}$ kpc, which they claim is the distance to the entirety of W31. Given that the source complexity within this region and the fact that G10.62-0.38 is almost a half degree from either W31-South or W31-North, we do not assign this maser distance to either source.

M17: There are two maser parallax measurements toward this region, consistent with each other to within the errors, one by Xu et al. (2011), who measured $1.98^{+0.14}_{-0.12}$ kpc and one by Chibueze et al. (2016), who measured $2.04^{+0.16}_{-0.17}$ kpc. We studied M17 in-depth in Paper II and adopted the value from Xu et al. (2011), which had slightly smaller errors. These values are also consistent with the near kinematic distances measured by multiple studies, for instance, the H87α+H88α transition measurements from Lockman (1989), which have a quoted $v_{lsr} = 16.8 \pm 0.3$ km s^{-1}, yield a kinematic near distance of $1.97^{+0.15}_{-0.38}$ kpc.

G20.733-0.087: This source only has kinematic measurements, and the v_{lsr} values all seem to hover in the 55.6–59.0 km s^{-1} range. There are four ATLASGAL clumps within $2'$ of these Galactic coordinates (Urquhart et al. 2018), three of which have v_{lsr} values in this range as well. However, there is one clump more than $1.'8$ from the Galactic coordinates with a $v_{lsr} = 103.3$ km s^{-1}. Consistent with this, Russeil (2003) detects a H$_2$CO transition here at 104 km s^{-1} as well as 56 km s^{-1}. Urquhart et al. (2018) claim the far distance is more likely due to H I self-absorption, and this far distance appears to be the general consensus (e.g., Russeil 2003; Quireza et al. 2006). Adopting the v_{lsr} of 55.96 ± 0.04 of Quireza et al. (2006) yields a kinematic far distance of $11.69^{+0.34}_{-0.44}$ kpc.

G29.944-0.042: The MSX images of this region from Conti & Crowther (2004) show a group of about six extended infrared sources all within a $4'$ radius. Zhang et al. (2014) present the velocity integrated ^{13}CO maps of this region from the Galactic Ring Survey (Jackson et al. 2006), revealing a single structure that encompasses all of the mid-infrared MSX sources centered very close to the galactic coordinates of this region. Zhang et al. (2014) also measure the parallax to two separate methanol maser sources within this ^{13}CO clump. The maser source G029.95-00.01, lies just under $2'$ from the Galactic coordinates, and has a parallax that yields a distance of $5.26^{+0.62}_{-0.50}$ kpc. The second maser source, G029.86-00.04, lies just over $5'$ from the Galactic coordinates, and has a parallax that yields a distance of $6.21^{+0.88}_{-0.69}$ kpc. Zhang et al. (2014) further state that because the distances and proper motions of G029.86-00.04 and G029.95-00.01 are consistent to within their uncertainties, they are likely located at the same distance, and they compute a variance-weighted average distance of $5.71^{+0.50}_{-0.42}$ kpc, which we adopt here. Consistent with this logic is the fact that both maser sources lie in the same ^{13}CO clump and that all of the ATLASGAL clumps within $8'$ of these Galactic coordinates have similar v_{lsr} values in the range of 95–101 km s^{-1} (Urquhart et al. 2018), which yield near kinematic distances of 5.7–6.2 kpc (which is consistent with the maser-derived distance).

W43: The distance to W43 was estimated by Zhang et al. (2014) based upon water and methanol maser parallaxes to two maser sources that lie approximately $-1.5°$ in Galactic longitude from W43 (i.e., the masers discussed above for G29.944-0.042), and two that lie approximately $+1.5°$ from W43 in longitude. Given that the molecular clumps found within this entire $3°$ area have very similar v_{lsr} values, it seems reasonable to assume that these masers, which are not coincident with W43, still provide a good distance estimate to W43. Zhang et al. (2014) estimate $5.49^{+0.39}_{-0.34}$ kpc based upon the average distance to the four methanol and water masers sources. We adopt this value in this work because it is the same value to within the errors of the spectrophotometrically derived distance from Moisés et al. (2011) of 4.90 ± 1.91 kpc. These values are also consistent to within the errors with the kinematically derived near distances quoted for this region, for example, the H91α transition velocity of 92.02 ± 0.04 km s^{-1} from Quireza et al. (2006), which yields a near kinematic distance of $5.57^{+0.38}_{-0.73}$ kpc.

G32.8+0.19: The distance to this source was derived from maser parallax observations of Zhang et al. (2019), which usually have accuracies of ± 1.0 kpc or less. However, this source distance is quoted with rather high errors. Zhang et al. (2019) quote two distance estimates using two different methods of converting the parallax to distance: $9.7^{+4.1}_{-2.2}$ kpc and $10.0^{+5.1}_{-2.7}$ kpc. This makes its status as a GH II unclear, since at 9.7 kpc the source has log $N_{LyC} = 49.90$ photons s^{-1}, and at 9.7+4.1 kpc it would have 50.15 photons s^{-1}. These maser distances are consistent (within their errors) with the far kinematic distance of $12.85^{+0.44}_{-0.34}$ kpc using a v_{lsr} value of 15.46 ± 0.15 km s^{-1} from Quireza et al. (2006) based on their measurements of the H91α transition. Given the high errors associated with the maser measurements, we will adopt this far kinematic distance in this work. Hou & Han (2014) list multiple v_{lsr} measurements toward this source from multiple groups, all of which have values of $v_{lsr} = 15.0–17.0$ km s^{-1}, but the measurement of Quireza et al. (2006) has the smallest error.

W49A: This source was covered in detail in De Buizer et al. 2021 (our Paper III). This source has reliable maser parallax measurements from Zhang et al. (2013) of $11.11^{+0.79}_{-0.69}$ kpc.

G48.596+0.042: There are two conflicting maser parallax measurements toward this region. Nagayama et al. (2011) measure a trigonometric parallax to the water masers in the source G48.61+0.02, which is ~$75''$ from the Galactic coordinates of this region and lies within the 6 cm radio-emitting diameter (i.e., $4.'2$), deriving a distance of 5.03 ± 0.19 kpc. On the contrary, Zhang et al. (2013) claim a distance to this same source as $10.75^{+0.61}_{-0.55}$ kpc also based upon water maser observations. Zhang et al. (2013) give multiple reasons to suspect the results of Nagayama et al. (2011), but such large discrepancies are not common.

The kinematic distance measurements toward this region all indicate a far distance of around 10 kpc, for instance, the H110α velocity from Araya et al. (2002) that is measured to be $v_{lsr} = 18.0 \pm 0.4$ km s^{-1}, which yields a far distance of $9.83^{+0.41}_{-0.44}$ kpc. Since this value is consistent to within the errors of the maser measurement of Zhang et al. (2013), we are inclined to believe it more and adopt it in this work. The near kinematic distance is only $1.21^{+0.35}_{-0.42}$ kpc, which means the distance of Nagayama et al. (2011) is incompatible with both the near and far kinematic distances. Therefore, the only way that the distance value of Nagayama et al. (2011) could be right was if G48.61+0.02 had a very high peculiar velocity.

G48.9-0.3: This source is a subregion of the very extensive W51 star-forming complex. Nagayama et al. (2015) derived a distance of $5.62^{+0.59}_{-0.49}$ kpc to this region based upon parallax observations of water masers in G48.99-0.30 (which we adopt

in this work). Even though G48.99-0.30 lies ~3′.5 from the galactic coordinates of this region ($\ell = 48.930$, $b = -0.286$), G48.9-0.3 is quite extended in both the radio ($D_{6\,cm} = 4′.4$) and mid-infrared ($D_{MSX22\,\mu m} \sim 9′$). Thus, G48.99-0.30 is likely to be at the same distance as the rest of the G48.9-0.3 region. Indeed, the list of v_{lsr} values compiled from multiple studies by Hou & Han (2014) for G48.99-0.30 ($v_{lsr} = 63$–67 km s^{-1}) almost exactly matches those for G48.9-0.3 ($v_{lsr} = 64$–67 km s^{-1}).

W51A: W51A contains two GH II regions, G49.5-0.4 and G49.4-0.3, separated by ~6′, both of which were covered in-depth in our Paper I. Trigonometric maser parallaxes were first measured toward G49.5-0.4 by Xu et al. (2009) using methanol masers, yielding a distance of $5.1^{+2.9}_{-1.4}$ kpc. These were followed by measurements of the water maser parallaxes by Sato et al. (2010), who obtained a much more precise value of $5.41^{+0.31}_{-0.28}$ kpc. We adopt this value for the distance to W51A:G49.5-0.4.

There have been no maser parallax measurements toward W51A:G49.4-0.3, but we adopt the same distance as G49.5-0.4, since they both display similar v_{lsr} values. Hou & Han (2014) compiled a list of v_{lsr} values from multiple studies and find a range of $v_{lsr} = 56$–59 km s^{-1} for G49.4-0.3, which is comparable to $v_{lsr} = 53$–55 km s^{-1} for G49.5-0.4 (with an outlier of 67.38 km s^{-1} in the H91α measurement of Quireza et al. 2006).

K3-50: This region is referred to as W58A in Conti & Crowther (2004). The distance to this region has been kinematically derived by multiple studies, with all derived values falling in the range of 7.3–9.3 kpc (e.g., Harris 1975; Balser et al. 2011; Ginsburg et al. 2011; also see discussion in Barnes et al. 2015), which places this region just outside the solar circle (with $R_{GC} > 8.3$ kpc) and in the outer Galaxy. The v_{lsr} measurements compiled by Hou & Han (2014) show a range between -23.11 and -26.22 km s^{-1}. The value from the H91α measurement of Quireza et al. (2006) of $v_{lsr} = -23.11 \pm 0.08$ km s^{-1} has the lowest error and yields a kinematic distance of $7.64^{+0.81}_{-0.54}$ kpc, which we adopt here. One exception is from Du et al. (2011), who measure a line at a comparable velocity (-23.3 km s^{-1}) but give a distance of 2.83 kpc, assigning it to the kinematic tangent point, which seems unlikely. Samal et al. (2010) were able to spectrally classify the star responsible for ionizing the K3-50D H II region (as an O4V star) and based upon its brightness and estimated extinction a distance of $8.5^{+1.5}_{-0.6}$ kpc was derived, which is inconsistent with the tangent point distance, and agrees with our more precise adopted distance to within the combined errors.

R7:DR7: Like K3-50, most previous observations of DR7 have yielded kinematic distances around 7–8 kpc, which places it just outside the solar circle and in the outer Galaxy. Hou & Han (2014) compiled a list of v_{lsr} values from multiple studies and find a range of $-42 < v_{lsr} < -37$ km s^{-1}. Measurement in the H91α transition by Quireza et al. (2006) yields a $v_{lsr} = -39.17 \pm 0.07$, which gives a kinematic distance of $7.30^{+0.84}_{-0.72}$ kpc. Du et al. (2011) also measure a line at -41 km s^{-1}, but assign the source to the tangent point distance of 1.56 kpc, which seems unlikely. With no spectrophotometric or maser parallax observations available, we adopt the kinematic distance of 7.30 kpc.

W3: W3 is located in the nearby Perseus Arm. Sources within this arm tend to have peculiar velocities, as evidenced by the difference in distance when derived via kinematic

measurements (~4 kpc, like that adopted by Conti & Crowther 2004) compared to ~2 kpc from spectrophotometric and trigonometric parallaxes (Navarete et al. 2019). A trigonometric maser parallax was measured toward W3(OH) by Xu et al. (2006), who derive a distance of 1.95 ± 0.04 kpc; however, this source is more than 16′ from W3 Main (which is the regions we are considering here). Navarete et al. (2019) use GAIA parallax measurements to show that different parts of the W3 star-forming complex appear to have slightly different distances. They obtain a distance to W3(OH) of $2.00^{+0.29}_{-0.23}$ kpc, which is consistent to within the errors with the maser-derived distances of Xu et al. (2006). However, for W3 Main Navarete et al. (2019) obtain a distance of $2.30^{+0.19}_{-0.16}$ kpc, which we adopt here.

RCW 42: This region is not well studied, and thus only kinematic distances are available. Using the H109+110α transition observations from Caswell & Haynes (1987) of $v_{lsr} = 39.0 \pm 1.0$ km s^{-1} (the only observation from Hou & Han 2014 with reported errors), we derive a kinematic distance of $5.97^{+0.90}_{-0.72}$ kpc and place it in the outer Galaxy. This value is consistent to within the errors of the value of 6.4 kpc adopted by Conti & Crowther (2004).

RCW 46: This source is also known as IRAS 10049-5657. Kinematically derived distance measurements vary between ~5 and 7 kpc (Vig et al. 2008), and this is due to the relatively large range in v_{lsr} measurements toward this location (19.0–26.2 km s^{-1}; Hou & Han 2014). The line measurement with the smallest error is 19.0 ± 1.0 km s^{-1} which yields a distance of $5.77^{+0.77}_{-0.77}$ kpc, based upon the radio recombination line measurements of Caswell & Haynes (1987). This source lies in the outer Galaxy, and therefore does not have a kinematic distance ambiguity. There does exist a spectro-photometric measurement of the distance toward this source by Moisés et al. (2011), who derive a value of 6.97 ± 2.72 kpc; however, the errors are quite large. We therefore adopt the 5.77 kpc value derived kinematically.

RCW 49: As one of the most luminous GH II regions in the southern hemisphere, RCW 49 has been heavily studied. The stellar cluster Westerlund 2 is believed to be contained within the H II region of RCW 49 and responsible for its ionization. The recent work of Tiwari et al. (2021) discusses the considerable variation of the accepted distance to this region over the decades, and we refer the reader to that work for the details. We will follow the recommendation of Tiwari et al. (2021) and adopt in this work the spectrophotometrically derived distance to Westerlund 2 of 4.16 ± 0.27 kpc from Vargas Álvarez et al. (2013) for RCW 49.

NGC 3372: This region is also known as the Carina Nebula. The luminous blue variable, η Carinae, is thought to be located within this nebula (Smith & Brooks 2008). From the expansion parallax of the Homunculus Nebula around η Car an accurate distance of 2.3 ± 0.1 kpc was found to the star (Smith 2006), and we adopt that distance here.

G289.066-0.357: Cersosimo et al. (2009) detected emission in the H166α transition from this region and determined a kinematic distance of 7.1 ± 0.3 kpc. This distance is consistent with the value we derive from the H109+110α transition measurements of Caswell & Haynes (1987), who find a $v_{lsr} = 19.0 \pm 1.0$ km s^{-1}, which we calculate to be $7.15^{+0.54}_{-0.93}$ kpc (which we adopt here). This source is outside the solar circle, and therefore there is no near/far distance ambiguity. One

outlier measurement is the distance of 3.1 kpc derived by Oliveira et al. (2018) using a color–magnitude diagram analysis of the Two Micron All Sky Survey sources found in the vicinity of G289.066-0.357. Such a near distance may mean the near-infrared stars used in the analysis are not associated with the radio region at all but instead are in the foreground.

NGC 3576: This source is also known as RCW 57 and IRAS 11097-6102. Binder & Povich (2018) have determined GAIA parallax observations toward stars believed to be associated with the ionized radio emission of NGC 3576. The value of 2.77 ± 0.31 kpc is close to the previously derived kinematic distances (e.g., de Pree et al. 1999), which place it to be at or near the tangent point of $\sim$3.0 kpc.

Contrarily, Moisés et al. (2011) spectrophotometrically derive a distance of 0.98 ± 0.19 kpc. Given that the distance derived via GAIA parallaxes is thought to be a more accurate method and it is consistent with the kinematic distance, we adopt that value in this work.

NGC 3603: There is a relatively large range of kinematic distances toward this region found in the literature ranging between 6 and 10 kpc (Kalari et al. 2019). Consistent with this, de Pree et al. (1999) found that the H90α velocities measured toward 13 subregions within NGC 3603 range between -2 and $+19$ km s^{-1}. They estimate a kinematic distance of 6.1 ± 0.6 kpc based upon the line velocity of $v_{lsr} = 9.1$ km s^{-1} found by integrating over the entire range of line velocities. Melena et al. (2008) performed spectroscopic parallax measurements toward multiple massive stars within NGC 3603 to derive a distance of 7.6 kpc. More recently, Drew et al. (2019) used GAIA parallaxes toward cluster members to derive a distance of 7.2 ± 0.1 kpc, which we adopt here.

G298.227-0.340/G298.862-0.438: These two sources ($\sim$0.6° apart) are the two brightest H II regions within a much larger star-forming complex called the Dragonfish Nebula (Russeil 1997) that resides in the outer Galaxy at a kinematically derived distance of $\sim$10 kpc. For example, using the v_{lsr} measured by Caswell & Haynes (1987) of 31.0 ± 1.0 km s^{-1} for G298.227-0.340 and 25.0 ± 1.0 km s^{-1} for G298.862-0.438 we obtain distances of $10.40^{+0.66}_{-0.66}$ kpc and $10.02^{+0.65}_{-0.58}$ kpc, respectively. This similarity indicates the two regions are likely part of the same physical region. de la Fuente et al. (2016) argue that the stellar cluster Mercer 30 is related to the Dragonfish Nebula and use spectrophotometric techniques to determine its distance as being 12.4 ± 1.7 kpc, which is consistent with the kinematic distances to within the errors. We adopt that distance here for both sources. Contrarily, Moisés et al. (2011) derive a spectrophotometric distance of 4.73 ± 1.78 kpc toward G298.227-0.340, which seems inconsistent with all other measurements.

G305.359+0.194: Binder & Povich (2018) have determined a distance to this region using GAIA parallax observations toward stars believed to be associated with the G305.359 +0.194 star-forming region. Their value of 3.59 ± 0.85 kpc agrees to within the errors with previously derived kinematic near distances of $\sim$3.4 kpc (e.g., Balser et al. 2015).

G319.158-0.398: Values of the v_{lsr} toward this region range between -16 and -27 km s^{-1} (e.g., Hou & Han 2014; Urquhart et al. 2018), which yield near/far kinematic values of $\sim$1.5/ 11.0 kpc. Urquhart et al. (2012) measure H I absorption toward this region and determine that the region is likely at the far kinematic distance. Using the measurement with the lowest error of -21.0 ± 1.0 km s^{-1} from the H109+110α observations of

Caswell & Haynes (1987) yields a far kinematic distance of $11.26^{+0.35}_{-0.42}$ kpc, which we adopt here.

G319.392-0.009: Values of the v_{lsr} toward this region range between -11 and -19 km s^{-1} (e.g., Hou & Han 2014; Urquhart et al. 2018), yielding near/far kinematic values of $\sim$1.0/11.5 kpc. Using the measurement with the lowest error of -14.0 ± 1.0 km s^{-1} from the H109+110α observations of Caswell & Haynes (1987) yields near/far kinematic distances of $1.01^{+0.23}_{-0.43}/11.78^{+0.34}_{-0.42}$ kpc. Since Urquhart et al. (2012) determine this region is at its far kinematic distance due to their measurements of H I absorption, we adopt the far kinematic distance of 11.78 kpc.

G320.327-0.184: This source is also known as IRAS 15061-5806. Urquhart et al. (2018) catalog five ATLASGAL clumps within 2′ of the galactic coordinates for this region with v_{lsr} values ranging between -6.9 and -11.1 km s^{-1}. They report that the kinematic distance ambiguity toward this region is resolved via H I absorption observations, which point to the near distance. This is contrary to the far distance listed by Conti & Crowther (2004), which is reported from Russeil (2003), who observe CO features up to -69 km s^{-1}. We adopt the near distance here of $0.64^{+0.38}_{-0.27}$ kpc based upon the v_{lsr} measurement of -11.0 ± 1.0 kpc from Caswell & Haynes (1987); however, we treat this source distance as still ambiguous given the conflicting absorption measurements.

RCW 97: The large GH II region of RCW 97 lies in the northern part of the G327.293-0.579 molecular cloud, which also contains an infrared dark cloud to the south (Wyrowski et al. 2006). Only kinematic estimates are available for the distance to this source, with line velocities in many transitions ranging from $-43.0 > v_{lsr} > -49.8$ km s^{-1} (e.g., Wyrowski et al. 2006; García et al. 2014; Hou & Han 2014; He et al. 2021). Both García et al. (2014) and Urquhart et al. (2012) determine this region is at its near kinematic distance due to the presence of absorption features like H I. Using the v_{lsr} measurement of -47.5 ± 0.1 kpc from the C^{18}O measurements of Wyrowski et al. (2006) yields our adopted distance of $2.98^{+0.23}_{-0.36}$ kpc.

G327.993-0.100: Urquhart et al. (2018) find three ATLAS-GAL clumps here within 45″ of each other and all three are contained in the infrared-emitting area as seen in the MSX data from Conti & Crowther (2004). Urquhart et al. (2018) claim from H I absorption analyses that two of these clumps have the larger kinematic distance of $\sim$11 kpc, while one has the near kinematic distance of $\sim$3 kpc. However, they also claim that these sources are all part of a cluster that is at 3.1 kpc. Further evidence that the region is at the near distance comes from Paladini et al. (2004), who claim this region is at the near kinematic distance because it has an optical counterpart. We will therefore adopt the near distance in this work as well. Using the v_{lsr} measurement of -45 ± 1.04 from the H109 +110α of Caswell & Haynes (1987) yields a distance of $2.80^{+0.31}_{-0.31}$ kpc.

G330.868-0.365: The range of v_{lsr} measurements to this region lie between -56.0 and -63.3 km s^{-1}. Jones & Dickey (2012), Paladini et al. (2004), and Urquhart et al. (2012) all determine a nearby distance from H I absorption observations. Using the value of -56.0 ± 1.0 km s^{-1} from the H109+110α observations of Caswell & Haynes (1987) yields a near distance of $3.44^{+0.37}_{-0.30}$ kpc, which we adopt here. Interestingly, Conti & Crowther (2004) use the far distance claimed by Russeil (2003), but it is unclear why the far distance is adopted

when all of their measured absorption features all have velocities similar to the v_{lsr} range mentioned above.

G331.324-0.348: Urquhart et al. (2018) show four ATLAS-GAL sources all with similar velocity ($-66.4 < v_{lsr} < -65.5$ km s^{-1}) all claimed to be in the same cluster at the near kinematic distance due to the presence of H I self-absorption. Paladini et al. (2004) also claim the near distance from their H I observations. Conti & Crowther (2004) use the far distance adopted by Russeil (2003) because they claim to see CO absorption at a very different velocity (-99 km s^{-1}). Spectrophotometric observations by Pinheiro et al. (2012) derive a distance of 3.29 ± 0.58 kpc, consistent with the near kinematic distance. We adopt the distance of Pinheiro et al. (2012) in this work.

G331.354+1.072: The H109+110α observations of Caswell & Haynes (1987) toward this region yield a v_{lsr} of -79 ± 1.0 kpc, consistent with other measured transitions. Urquhart et al. (2018) find one ATLASGAL clump with $2'$ of the galactic coordinates of this region and measure a v_{lsr} of -78.3 km s^{-1} and assume near kinematic distance due to this region's high galactic latitude. Though the H I absorption observations from Jones & Dickey (2012) were ambiguous, Urquhart et al. (2012) measure H I absorption consistent with the near distance as well. We therefore adopt the near distance in this work, and using the v_{lsr} of Caswell & Haynes (1987), derive a distance of $4.50^{+0.55}_{-0.34}$ kpc.

G331.529-0.084: Only kinematic measurements have been made toward this region and the distance is highly uncertain. Urquhart et al. (2018) find four ATLASGAL molecular clumps within $2'$ of the radio coordinates for this source, all with comparable v_{lsr} values ranging from -87.3 to -89.2 km s^{-1}. However, only one of these clumps has H I absorption measurements consistent with the far distance, while the remaining three are claimed to be too ambiguous to solve. Nonetheless, Urquhart et al. (2018) consider the source as part of the same cluster and places them at the near kinematic distance. García et al. (2014) state they resolved the distance ambiguity to be near based upon H$_2$CO absorption measurements, but Paladini et al. (2004) claim the far kinematic distance based upon H I absorption measurements. Yet others (e.g., Jones & Dickey 2012) claim that the source is at the kinematic tangent point. Merello et al. (2013) describe the prior distance measurements in detail and decide that the region is likely at the tangent point as well and choose to use a large uncertainty of 30% given by the near and far kinematic distances. We will employ that strategy here. The v_{lsr} measurements compiled by Hou & Han (2014) show a range between -88.4 and -90.6 km s^{-1}, with an outlier of -100.7 km s^{-1} from the CS observations of Bronfman et al. (1996). Using the H109+110α observations of Caswell & Haynes (1987) of v_{lsr} of -89 ± 1.0 kpc, gives a near distance of $5.11^{+0.60}_{-0.47}$ kpc and a far distance of $9.48^{+0.50}_{-0.58}$ kpc. However, we will adopt the tangent point distance of 7.31 ± 2.19 kpc, with the large errors to reflect the near/far distances. Despite all of this doubt in distance, we will point out that this region is so bright that even at the near kinematic distance, G331.529-0.084 would still qualify as a GH II region.

G333.122-0.446: This is the first of three sources on our list that are believed to be colocated within the G333 giant molecular cloud, one of the most massive in the fourth quadrant of the Galaxy (Wiles et al. 2016). Urquhart et al. (2018) find three ATLASGAL sources, assumed to be in a cluster at near

kinematic distance. The H I absorption measurements of Jones & Dickey (2012) and Urquhart et al. (2012) are consistent with a near kinematic distance, and Paladini et al. (2004) claim the near distance because this H II region has an optical component. Given the v_{lsr} of this region (e.g., -52 ± 1.0 km s^{-1} from Caswell & Haynes 1987) a near kinematic distance would be $\sim$3.3 kpc. However, an even nearer and more accurate distance was measured by Figuerêdo et al. (2005) via spectrophotometric techniques of 2.6 ± 0.2 kpc. Later spectrophotometric measurements by Moisés et al. (2011) yielded a value of 3.57 ± 1.33 kpc, which is consistent with the value from Figuerêdo et al. (2005) to within the errors. As even Moisés et al. (2011) point out, the results from Figuerêdo et al. (2005) are more reliable, and thus we adopt their distance here. This distance is also consistent with the distances measured toward the other two sources in the G333 complex (G333.293-0.382 and G333.610-0.217 discussed below), signifying that they may indeed be related.

G333.293-0.382: This is the second of three sources on our list that are believed to reside within the G333 giant molecular cloud. Urquhart et al. (2018) find three ATLASGAL sources within $2'$ of the galactic coordinates of this source, and claim they are in a cluster at the near kinematic distance due to the H I absorption observations of Urquhart et al. (2012). García et al. (2014) and Paladini et al. (2004) also both claim the near distance as well due to the presence of an optical component associated with the H II region here. We derive a near distance of $\sim$3.2 kpc toward this region using typical v_{lsr} values toward this region (e.g., -50 ± 1.0 km s^{-1} from Caswell & Haynes 1987). At this distance G333.293-0.382 just makes it over the criterion of being a GH II region ($\log N_{LyC} = 50.00$ photons s^{-1}). However, the spectrophotometric results of Roman-Lopes et al. (2009) toward the associated source IRAS 161775018IRS1 derive a distance of at most 2.6 ± 0.7 kpc given the best match of their spectra to a O3If* supergiant. However, they point out that such stars in star formation regions are rare, and that the distance would be 1.2 ± 0.7 kpc if one assumes the source to instead be an O3V-O5V main-sequence star. This closer distance is much smaller than the kinematic distance; however, either of these two distances would put G333.293-0.382 out of contention for being a GH II region. We will adopt here the larger spectrophotometric distance (being that it is closer to the kinematic distance) of 2.6 kpc, which leads to a $\log N_{LyC} = 49.79$ photons s^{-1} and is consistent with the distances measured to the two other regions within the G333 complex, G333.122-0.446 and G333.610-0.217.

G333.610-0.217: This is the third of three sources on our list that are believed to be colocated within the G333 giant molecular cloud, and is the most prominent and best studied among the three (e.g., Townsley et al. 2014; Ramírez-Tannus et al. 2020). This source is associated with the H II region known as RCW 106. H I absorption measurements of Paladini et al. (2004), and Urquhart et al. (2012) point to a near kinematic distance. However, Ramírez-Tannus et al. (2020) derive a distance of 2.54 ± 0.71 kpc from GAIA parallax measurements of cluster members within G333.6-0.2, which we adopt here. This distance is in agreement with the reported distances of both G333.122-0.446 and G333.293-0.382 above, again implying they are all indeed colocated within the G333 giant molecular cloud.

G338.398+0.164: The galactic coordinates of this source are close to that of the star cluster Mercer 81 ($\ell = 338.384$, $b = 0.111$) toward which Davies et al. (2012) performed a

kinematic analysis placing the cluster close to where the far end of the Galactic Bar intersects the Norma spiral arm at a distance of 11 ± 2 kpc. There is still some confusion regarding distance, however, shown by Urquhart et al. (2018), who find four ATLASGAL sources within $2'$ of the galactic coordinates of this source, and claim they are in a cluster at the near kinematic distance (2.7 kpc) due to the H I absorption observations. However, of the four ATLASGAL sources, the one closest to the galactic coordinates of G338.398+0.164 is shown by Urquhart et al. (2012) to have H I absorption in keeping with the far distance, one source is thought to be at the near distance, and the remaining two are too ambiguous to decide. Given all of the uncertainty, we will tentatively adopt the far distance indicated by the ATLASGAL source closest to the coordinates of this source. Using the value of -29.0 ± 1.0 km s^{-1} from the H109+110α observations of Caswell & Haynes (1987) we derive a far distance of $13.29^{+0.25}_{-0.45}$ kpc, which we adopt here.

G338.400-0.201: This region is not studied very well, and there are only a handful of observations from which to assess the distance (with conflicting results). Wilson et al. (1970) find a value of $v_{\mathrm{lsr}} = -4.3 \pm 3.6$ km s^{-1} in the H109α transition, while Caswell & Haynes (1987) measure 2.0 ± 1.0 km s^{-1} in the similar H109+110α transition. Meanwhile, Urquhart et al. (2007) measure a ^{13}CO v_{lsr} of 4.0 km s^{-1}. At positive velocities, the region exists in the outer Galaxy (as argued by Jones & Dickey 2012), and thus has no distance ambiguity. For v_{lsr} values at the more negative end of the measured range, there is a chance the source could have a very close (>0.5 kpc) near kinematic distance. The MSX 22 μm images of Conti & Crowther (2004) show a relatively faint source at this location, with an FWHM $< 1'$. Such an underwhelming infrared region may indicate that the source is a modest H II region at the near distance and not a distant GH II region, which tends to have more complex and extended morphologies (as discussed for Sgr D and W42 in Section 6). However, without more evidence we will not dismiss the source as a candidate GH II region and will tentatively use the Caswell & Haynes (1987) v_{lsr}, which leads to an outer Galaxy kinematic distance of $15.71^{+0.58}_{-0.40}$ kpc.

G345.555-0.043: This region is known as the G345.555-0.042 GMC complex (Urquhart et al. 2012), but is not well studied. There are two ATLASGAL submillimeter clumps within $2'$ of these galactic coordinates of this region, both of these clumps lie $\sim 1\!'\!.7$ away. Russeil (2003) and Caswell & Haynes (1987) find CO and H$_2$CO transitions at much higher absolute velocities than the $v_{\mathrm{lsr}} = -6.0 \pm 1.0$ km s^{-1} derived from H109+110α observations of Caswell & Haynes (1987), and thus claim the far kinematic distance to this region. Using that v_{lsr} value we derive a far distance of $15.28^{+0.57}_{-0.35}$ kpc, which we adopt here.

G345.645+0.009: This source has a radio-emitting size of $\theta_{6\,\mathrm{cm}} = 4\!'\!.2$ according to Conti & Crowther (2004). Urquhart et al. (2018) find four ATLASGAL molecular clumps within this radio source area, all with comparable v_{lsr} values (-6.0 to -10 km s^{-1}). However, two of these clumps have H I absorption measurements consistent with the near distance and two have H I absorption measurements consistent with the far distance. The infrared source at the center of the radio emission is only $1\!'\!.9$ in diameter in the 22 μm MSX images (Conti & Crowther 2004), and the only one ATLASGAL clump is contained within that region, and that clump is one determined to be at the far kinematic distance due to H I absorption measurement (Urquhart et al. 2012). Using the

$v_{\mathrm{lsr}} = -10.0 \pm 1.0$ km s^{-1} value derived from H109+110α observations of Caswell & Haynes (1987) we derive a far distance of $14.97^{+0.39}_{-0.45}$ kpc, which we adopt here.

G347.611+0.204: This source has a 6 cm radio-emitting diameter of $6\!'\!.1$ according to Conti & Crowther (2004). Like our previous example, Urquhart et al. (2018) find multiple ATLASGAL molecular clumps within this radio source area, totaling five clumps all with comparable v_{lsr} values (-91 to -97 km s^{-1}). One of these clumps has H I absorption measurements consistent with the near distance, one with the far distance, and three are too ambiguous to determine. The stellar cluster (DBS2003) 179 (Dutra et al. 2003) is believed to be associated with the H II emission here. Borissova et al. (2012) provide a good overview of the history of distance measurements toward G347.611+0.204 and derive a spectro-photometric distance of 7.9 ± 0.8 kpc, which we adopt here. This distance is consistent with the near kinematic distance of ~ 7.0 kpc.

G351.467-0.462: Urquhart et al. (2018) find three ATLAS-GAL sources within $2'$ of these galactic coordinates all at the same velocity ($v_{\mathrm{lsr}} = -22$ to -23 km s^{-1}) and assume these to be a related cluster at a near kinematic distance due to H I absorption. This is supported by a similar measurement by Quireza et al. (2006), though Jones et al. (2013) say their H I absorption spectrum does not conclusively point one way or the other. Borissova et al. (2006) derive a spectrophotometric distance to the region by studying a stellar cluster that is coincident with the ionized gas in this region. They calculate a distance ~ 3.2 kpc but report no formal no uncertainty. Using the v_{lsr} measurements of the H91α transition toward this source by Quireza et al. (2006) of -21.44 ± 0.74 km s^{-1} yields a near kinematic distance of $3.24^{+0.34}_{-0.26}$ kpc, which we will adopt here because it is consistent with the spectrophotometric distance determination.

Sgr C: As pointed out by Kendrew et al. (2013), the v_{lsr} of Sgr C is very similar to those of sources in the Near 3 kpc Arm at a distance of ~ 5.5 kpc, which complicates kinematic interpretations. That being said, measured v_{lsr} values, like those of Caswell & Haynes (1987; -60 ± 1.0 km s^{-1} from the measured H109+110α transitions) yield tangent point kinematic distances ($8.34^{+0.15}_{-0.17}$ kpc) that agree with the distance to the Galactic Center to within the errors.

ORCID iDs

James M. De Buizer ⓘ https://orcid.org/0000-0001-7378-4430
Wanggi Lim ⓘ https://orcid.org/0000-0003-4243-6809
Nicole Karnath ⓘ https://orcid.org/0000-0003-3682-854X
James T. Radomski ⓘ https://orcid.org/0000-0003-0740-2259
Lars Bonne ⓘ https://orcid.org/0000-0002-0915-4853

References

Ai, M., Zhu, M., Xiao, L., et al. 2013, RAA, 13, 935
Anderson, L. D., & Bania, T. M. 2009, ApJ, 690, 706
Araya, E., Hofner, P., Churchwell, E., et al. 2002, ApJS, 138, 63
Arias, J. I., Barbá, R. H., Maíz Apellániz, J., et al. 2006, MNRAS, 366, 739
Balega, Y. Y., Chentsov, E. L., Leushin, V. V., et al. 2014, AstBu, 69, 46
Balser, D. S., Rood, R. T., Bania, T. M., et al. 2011, ApJ, 738, 27
Balser, D. S., Wenger, T. V., Anderson, L. D., et al. 2015, ApJ, 806, 199
Barbosa, C. L., Blum, R. D., Damineli, A., et al. 2016, ApJ, 825, 54
Barnes, P., Li, D., Telesco, C., et al. 2015, MNRAS, 453, 2622
Binder, B. A., & Povich, M. S. 2018, ApJ, 864, 136
Blum, R. D., Conti, P. S., & Damineli, A. 2000, AJ, 119, 1860

Blum, R. D., & Damineli, A. 1999, ApJ, 512, 237
Blum, R. D., Damineli, A., & Conti, P. S. 2001, AJ, 121, 3149
Borissova, J., Georgiev, L., Hanson, M. M., et al. 2012, A&A, 546, A110
Borissova, J., Ivanov, V. D., Minniti, D., et al. 2006, A&A, 455, 923
Bronfman, L., Nyman, L.-A., & May, J. 1996, A&AS, 115, 81
Caswell, J. L., & Haynes, R. F. 1987, A&A, 171, 261
Cersosimo, J. C., Mader, S., Figueroa, N. S., et al. 2009, ApJ, 699, 469
Chibueze, J. O., Kamezaki, T., Omodaka, T., et al. 2016, MNRAS, 460, 1839
Churchwell, E., Smith, L. F., Mathis, J., et al. 1978, A&A, 70, 719
Clarke, M., Vacca, W. D., & Shuping, R. Y. 2015, in ASP Conf. Ser. 495, Astronomical Data Analysis Software an Systems XXIV (ADASS XXIV), ed. A. R. Taylor & E. Rosolowsky (San Francisco, CA: ASP), 355
Conti, P. S., & Crowther, P. A. 2004, MNRAS, 355, 08367
Corbel, S., & Eikenberry, S. S. 2004, A&A, 419, 191
Damiani, F., Prisinzano, L., Micela, G., et al. 2019, A&A, 623, A25
Davies, B., de La Fuente, D., Najarro, F., et al. 2012, MNRAS, 419, 1860
De Buizer, J. M., Lim, W., Liu, M., et al. 2021, ApJ, 923, 198
de la Fuente, D., Najarro, F., Borissova, J., et al. 2016, A&A, 589, A69
de Pree, C. G., Nysewander, M. C., & Goss, W. M. 1999, AJ, 117, 2902
Deharveng, L., Zavagno, A., Samal, M. R., et al. 2015, A&A, 582, A1
Dewangan, L. K., Luna, A., Ojha, D. K., et al. 2015a, ApJ, 811, 79
Dewangan, L. K., Mayya, Y. D., Luna, A., et al. 2015b, ApJ, 803, 100
Dewangan, L. K., Sano, H., Enokiya, R., et al. 2019, ApJ, 878, 26
Downes, D., Wilson, T. L., Bieging, J., et al. 1980, A&AS, 40, 379
Drew, J. E., Monguió, M., & Wright, N. J. 2019, MNRAS, 486, 1034
Du, Z. M., Zhou, J. J., Esimbek, J., et al. 2011, A&A, 532, A127
Dutra, C. M., Bica, E., Soares, J., et al. 2003, A&A, 400, 533
Eisenhauer, F., Quirrenbach, A., Zinnecker, H., et al. 1998, ApJ, 498, 278
Elia, D., Molinari, S., Schisano, E., et al. 2017, MNRAS, 471, 100
Figuerêdo, E., Blum, R. D., Damineli, A., et al. 2005, AJ, 129, 1523
Garay, G., Rodriguez, L. F., Moran, J. M., et al. 1993, ApJ, 418, 368
García, P., Bronfman, L., & Nyman, L.-Å. 2014, ApJS, 212, 2
Ginsburg, A., Darling, J., Battersby, C., et al. 2011, ApJ, 736, 149
Gutermuth, R. A., Megeath, S. T., Myers, P. C., et al. 2009, ApJS, 184, 18
Harris, S. 1975, MNRAS, 170, 139
He, Y.-X., Henkel, C., Zhou, J.-J., et al. 2021, ApJS, 253, 2
Herter, T. L., Vacca, W. D., Adams, J. D., et al. 2013, PASP, 125, 1393
Hillenbrand, L. A. 1997, AJ, 113, 1733
Hoffmeister, V. H., Chini, R., Scheyda, C. M., et al. 2008, ApJ, 686, 310
Hou, L. G., & Han, J. L. 2014, A&A, 569, A125
Inoue, A. K., Hirashita, H., & Kamaya, H. 2001, ApJ, 555, 613
Jackson, J. M., Rathborne, J. M., Shah, R. Y., et al. 2006, ApJS, 163, 145
Jones, C., & Dickey, J. M. 2012, ApJ, 753, 62
Jones, C., Dickey, J. M., Dawson, J. R., et al. 2013, ApJ, 774, 117
Kalari, V. M., Vink, J. S., de Wit, W. J., et al. 2019, A&A, 625, L2
Kassis, M., Deutsch, L. K., Campbell, M. F., et al. 2002, AJ, 124, 1636
Kazes, I., & Aubry, D. 1973, A&A, 22, 413
Kendrew, S., Ginsburg, A., Johnston, K., et al. 2013, ApJL, 775, L50
Lim, W., & De Buizer, J. M. 2019, ApJ, 873, 51
Lim, W., De Buizer, J. M., & Radomski, J. T. 2020, ApJ, 888, 98
Lockman, F. J. 1989, ApJS, 71, 469
Mehringer, D. M., Goss, W. M., Lis, D. C., et al. 1998, ApJ, 493, 274
Melena, N. W., Massey, P., Morrell, N. I., et al. 2008, AJ, 135, 878
Merello, M., Bronfman, L., Garay, G., et al. 2013, ApJ, 774, 38
Mezger, P. G. 1970, in IAU Symp. 38, The Spiral Structure of Our Galaxy, 107
Mezger, P. G., & Henderson, A. P. 1967, ApJ, 147, 471
Mezger, P. G., Smith, L. F., & Churchwell, E. 1974, A&A, 32, 269
Moisés, A. P., Damineli, A., Figuerêdo, E., et al. 2011, MNRAS, 411, 705

Molinari, S., Schisano, E., Elia, D., et al. 2016, A&A, 591, 149
Nagayama, T., Kobayashi, H., Omodaka, T., et al. 2015, PASJ, 67, 65
Nagayama, T., Omodaka, T., Handa, T., et al. 2011, PASJ, 63, 719
Navarete, F., Galli, P. A. B., & Damineli, A. 2019, MNRAS, 487, 2771
Odenwald, S. F. 1989, in IAU Symp. 136, The Center of the Galaxy, ed. M. Morris (Dordrecht: Kluwer), 205
Oliveira, R. A. P., Bica, E., & Bonatto, C. 2018, MNRAS, 476, 842
Paladini, R., Davies, R. D., & De Zotti, G. 2004, MNRAS, 347, 237
Panagia, N. 1973, AJ, 78, 929
Pinheiro, M. C., Abraham, Z., Copetti, M. V. F., et al. 2012, MNRAS, 423, 2425
Purcell, C. R., Hoare, M. G., Cotton, W. D., et al. 2013, ApJS, 205, 1
Quireza, C., Rood, R. T., Bania, T. M., et al. 2006, ApJ, 653, 1226
Ramírez-Tannus, M. C., Poorta, J., Bik, A., et al. 2020, A&A, 633, A155
Rathborne, J. M., Whitaker, J. S., Jackson, J. M., et al. 2016, PASA, 33, e030
Reid, M. J., Menten, K. M., Brunthaler, A., et al. 2014, ApJ, 783, 130
Reid, M. J., Menten, K. M., Zheng, X. W., et al. 2009, ApJ, 705, 1548
Rickert, M., Yusef-Zadeh, F., & Ott, J. 2019, MNRAS, 482, 5349
Roman-Lopes, A., Abraham, Z., Ortiz, R., et al. 2009, MNRAS, 394, 467
Russeil, D. 1997, A&A, 319, 788
Russeil, D. 2003, A&A, 397, 133
Sakai, D., Oyama, T., Nagayama, T., et al. 2017, PASJ, 69, 64
Samal, M. R., Pandey, A. K., Ojha, D. K., et al. 2010, ApJ, 714, 1015
Sanna, A., Reid, M. J., Menten, K. M., et al. 2014, ApJ, 781, 108
Sato, M., Reid, M. J., Brunthaler, A., et al. 2010, ApJ, 720, 1055
Schraml, J., & Mezger, P. G. 1969, ApJ, 156, 269
Shields, G. A. 1990, ARA&A, 28, 525
Simpson, J. P., Colgan, S. W. J., Cotera, A. S., et al. 2021, ApJ, 910, 59
Smith, L. F., Biermann, P., & Mezger, P. G. 1978, A&A, 66, 65
Smith, N. 2006, MNRAS, 367, 763
Smith, N., & Brooks, K. J. 2008, in Handbook of Star Forming Regions, ed. B. Reipurth, Vol. II, 138
Smith, N., Jackson, J. M., Kraemer, K. E., et al. 2000, ApJ, 540, 316
Szymczak, M., Wolak, P., Bartkiewicz, A., et al. 2012, AN, 333, 634
Tiwari, M., Karim, R., Pound, M. W., et al. 2021, ApJ, 914, 117
Townsley, L. K., Broos, P. S., Garmire, G. P., et al. 2014, ApJS, 213, 1
Urquhart, J. S., Busfield, A. L., Hoare, M. G., et al. 2007, A&A, 474, 891
Urquhart, J. S., Hoare, M. G., Lumsden, S. L., et al. 2012, MNRAS, 420, 1656
Urquhart, J. S., König, C., Giannetti, A., et al. 2018, MNRAS, 473, 1059
Vargas Álvarez, C. A., Kobulnicky, H. A., Bradley, D. R., et al. 2013, AJ, 145, 125
VERA Collaboration, Hirota, T., & Nagayama, T. 2020, PASJ, 72, 50
Vig, S., Ghosh, S. K., Ojha, D. K., et al. 2008, AJ, 136, 1427
Wenger, T. V., Balser, D. S., Anderson, L. D., et al. 2018, ApJ, 856, 52
Wenger, T. V., Balser, D. S., Anderson, L. D., et al. 2019, ApJ, 887, 114
Wiles, B., Lo, N., Redman, M. P., et al. 2016, MNRAS, 458, 3429
Wilson, T. L. 1974, A&A, 31, 83
Wilson, T. L., Mezger, P. G., Gardner, F. F., et al. 1970, A&A, 6, 364
Wink, J. E., Wilson, T. L., & Bieging, J. H. 1983, A&A, 127, 211
Wyrowski, F., Menten, K. M., Schilke, P., et al. 2006, A&A, 454, L91
Xu, Y., Moscadelli, L., Reid, M. J., et al. 2011, ApJ, 733, 25
Xu, Y., Reid, M. J., Menten, K. M., et al. 2009, ApJ, 693, 413
Xu, Y., Reid, M. J., Zheng, X. W., et al. 2006, Sci, 311, 54
Zhang, B., Moscadelli, L., Sato, M., et al. 2014, ApJ, 781, 89
Zhang, B., Reid, M. J., Menten, K. M., et al. 2013, ApJ, 775, 79
Zhang, B., Reid, M. J., Zhang, L., et al. 2019, AJ, 157, 200
Zhang, Y., & Tan, J. C. 2011, ApJ, 733, 55